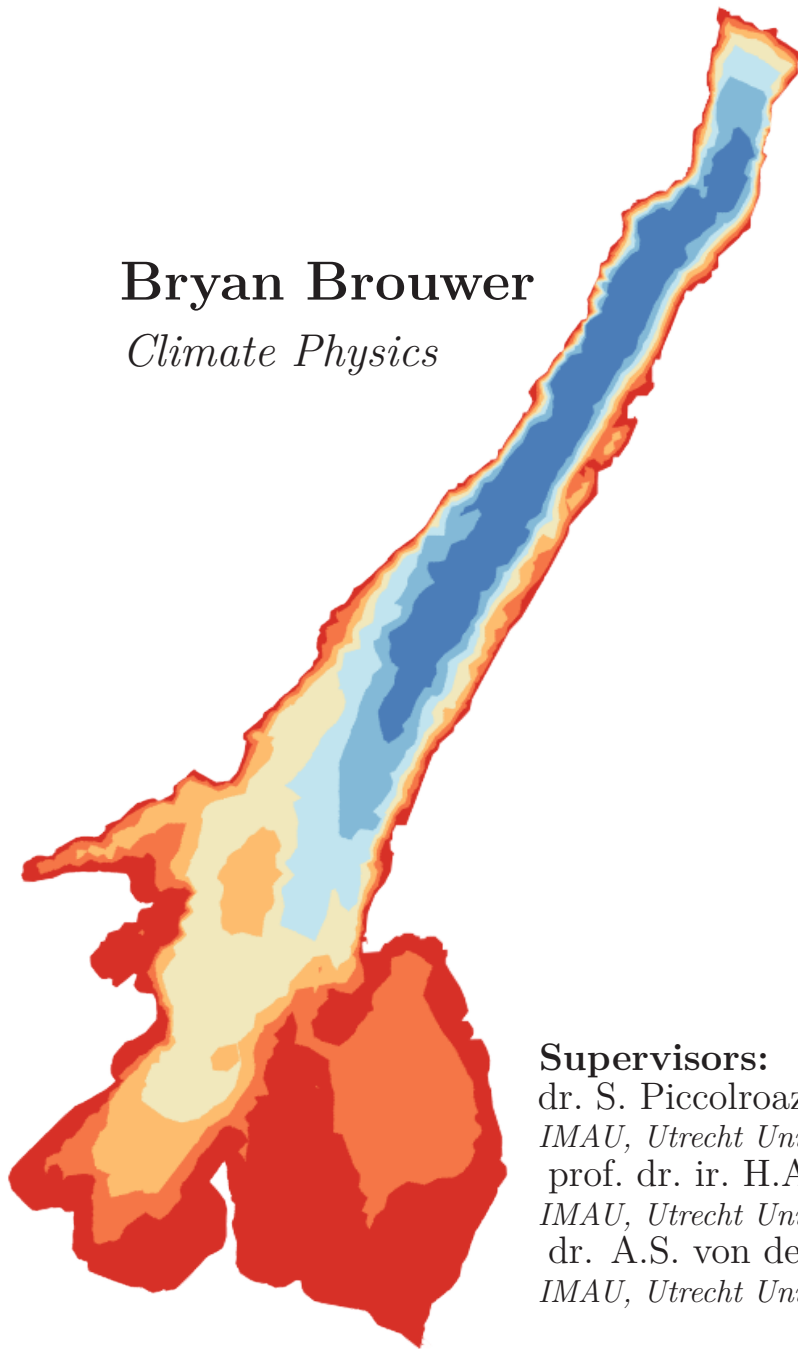# Seasonal variability of mixing in northern Lake Garda

Bryan Brouwer

Climate Physics

Supervisors:
dr. S. Piccolroaz
IMAU, Utrecht University
 prof. dr. ir. H.A. Dijkstra
IMAU, Utrecht University
 dr. A.S. von der Heydt
IMAU, Utrecht University

Abstract

Mixing is a very important physical mechanism in lakes, since it is strongly connected to turbulence. Turbulence has a direct influence on thermal stratification and biological processes. This study used in-situ observations to investigate the seasonal variability of mixing in northern Lake Garda (Italy). The in-situ observations were made using a vertical microstructure profiler (MicroCTD, Rockland Scientific International), which measured temperature, conductivity, turbidity, chlorophyll-a concentrations and vertical shear. These measurements were performed on a monthly basis, starting in March 2017, for a whole year. Four different stations were monitored at the same time. Three of them were forming a cross section perpendicular to lake's main axis, which is oriented in a northeast-southwest direction. The fourth station was located further to the south. Additionally, measurements of meteorological variables were obtained from nearby meteorological ground stations. The combination of all these measurements made it possible to quantify which external forcing mechanisms had the most influence on the dynamics occurring in the lake throughout the year. It was found that throughout the year the surface buoyancy flux is the most important source of Turbulent Kinetic Energy (TKE), except during occasional extreme wind events, which caused significant amounts of TKE to be produced. Observations suggested the development of a secondary circulation, after persistent, unidirectional winds, causing coastal up-/downwelling along the narrow and deep part of the lake. It was found that a transition period from negative to positive buoyancy fluxes in the months September and October marked a transition in the wind climate and caused the development of an unstable boundary layer in the air above the lake. This transition period was accompanied by a second algal bloom and was the onset of Mixed Layer deepening. During the months December until March a continuous cooling of the upper layer was observed. The mixing dynamics in the lake turned out to be more event-based and did not follow any clear seasonal pattern.

Contents

Chapter 1

Introduction

Mixing is of vital importance in lakes and other bodies of water, since it influences the rates at which chemical and biological processes take place [1][2]. It depends strongly on physical quantities like thermal stratification, heat- and momentum fluxes and is strongly associated with turbulence created by these fluxes. Even though lakes are commonly more extended in the horizontal directions than in the vertical direction the vertical stratification is of importance, because it slows down vertical mixing and this causes vertical mixing to be slower than horizontal mixing [3].

Increased temperatures due to climate change might change the thermal stratification in lakes [4][5] and possibly the heat flux. Since mixing is depending on these factors, climate change may change the mixing characteristics of lakes. Furthermore, climate change may change the timing of the growth of phytoplankton, which will subsequently affect the ecosystems in lakes and may cause regime change in foodwebs [6]. The timing of phytoplankton growth is mostly controlled by factors like solar radiation and vertical mixing [7]. For deep lakes it was shown that it is mostly controlled by vertical mixing [8].

A recent study already found an ecological shift in the past three decades due to climate change and a decrease in the amount of Deep Mixing Events in Lake Garda, a deep lake [9]. These events enhance the distribution of nutrients and determine (bio)geochemical processes occurring in deep lakes [10]. In order to understand the dynamics occurring in a lake on an interannual or decadal timescale, it is therefore crucial to understand how quantities like stratification and heat- and momentum fluxes affect turbulence and thus mixing on an annual timescale.

The study on the dynamics of physical, chemical and biological processes on lakes on a seasonal timescale is often limited by either low-sampling frequencies or sampling during relatively short periods of the year. Over the years, though, many comprehensive studies have been performed on lakes all over the world to study these processes over a seasonal cycle, for example on the Great Slave Lake [11]. Mixing dynamics in particular, have been investigated on i.e. Lake Geneva [12], a deep lake, and more recently on Lake Scharmützelsee and Lake Arendsee [13]. There are also studies which investigate external forcing and mixing in lakes, for example in the deep mountain lake Lake Redó in the Pyrenees [14]. However, there are not many studies that investigate external forcing in relation to turbulence and mixing in lakes on an annual timescale.

The objective of this study was to determine the temporal evolution of quantities related to mixing, like the Turbulent Kinetic Energy dissipation and the vertical mix-

ing coefficient, but also of lake temperature and chlorophyll-*a* over a full seasonal cycle in Lake Garda, a deep alpine lake. We will discuss whether these quantities possess a seasonal cycle or are more event-based. These quantities were determined with the help of in-situ measurements obtained by a free-falling vertical microstructure profiler (MicroCTD, Rockland Scientific International). The obtained data will also be coupled to meteorological data from nearby weather stations to quantify which external forcing mechanisms had the most influence on the dynamics occurring in the lake throughout the year. Specifically we will assess the influence of air temperature, net surface heat flux and wind on vertical mixing, lake temperature and chlorophyll-*a* concentrations in Lake Garda on an annual timescale.

Lake Garda is of particular interest as a deep alpine lake, because it consists of two different parts. The northern part of the lake is narrower (4 km on average) and deeper than the southern part and is surrounded by mountains. Due to these mountains the winds in the northern part of the lake are mostly along the main axis of the lake in this part, which is oriented in a northeast-southwest fashion [15]. The bathymetry in the northern part of the lake is relatively regular and uniform as well. Therefore Lake Garda forms a natural laboratory to study the relation between mixing in the upper water column, phytoplankton concentrations and external forcing mechanisms.

Lake Garda is the largest freshwater lake in Italy. Its maximum depth is 346 m, while it has a surface area of around 370 km^2 and a volume of 49 km^3. The main inflow of the lake is the Sarca river at the northern edge. The outflow is the river Mincio at the southern part of the lake and it has been found that the renewal time of the lake is about 27 years [16]. The lake is located in the northern part of Italy (45.6°N, 10.6°E) at the southern edge of the Alps.

Lake Garda is characterized as a oligotrophic to mesotrophic lake [17][18]. Therefore Lake Garda has relatively clear water and low to moderate primary productivity and nutrient concentrations. The lake is also considered to be oligomictic [16], which means that the lake will undergo incomplete mixing during variable periods. Occasionally, mostly during cold winters, a complete mixing of the water column may occur.

Chapter 2

Theory & Methods

2.1 Generation of turbulence

Mixing[1] is the result of turbulence associated with advective motions. So to describe mixing we need to look at the energy associated with turbulence, the so-called Turbulent Kinetic Energy (TKE). To derive an equation for the Turbulent Kinetic Energy, one should start from the Navier-Stokes equations. The Navier-Stokes equations for a viscous, incompressible fluid on a non-rotating Earth can be expressed as:

$$\frac{\partial u_i}{\partial t} + \sum_{j=1}^{3} \frac{\partial u_i}{\partial x_j} = -\delta_{i3}g - \frac{1}{\rho_w}\frac{\partial p}{\partial x_i} + \nu \sum_{j=1}^{3} \frac{\partial^2 u_i}{\partial x_j^2} \tag{2.1}$$

with u_i the velocity component in the Cartesian direction x_i for $i = 1 - 3$, respectively. x_3 is the upward direction and t is time. δ_{i3} denotes a Kronecker Delta. It is equal to 1 if $i = 3$ and 0 otherwise. p is the pressure, ν the kinematic viscosity, g the acceleration due to gravity and ρ_w the density of water. Additionally we can write the continuity equation as:

$$\sum_{i=1}^{3} \frac{\partial u_i}{\partial x_i} = 0 \tag{2.2}$$

In order to separate the mean flow from the turbulent flow, we split all variables (p, ρ_w and u_i) in two parts. A temporal mean, $\overline{f}$, and a fluctuation about the mean, f': $f = \overline{f} + f'$, with f some random variable. The temporal mean is defined as:

$$\overline{f} = \frac{1}{T} \int_{t-T/2}^{t+T/2} f(t')dt' \tag{2.3}$$

where T is a suitable time interval for averaging and t' a dummy variable used for integration purposes only.

---

[1]This section is based on Imboden and Wüest [19], unless stated otherwise.

Applying the above-mentioned splitting of variables to Equation 2.1 and taking the temporal mean of the equations, we obtain:

$$\frac{\partial \overline{u_i}}{\partial t} + \sum_{j=1}^{3} \overline{u_j} \frac{\partial u_i}{\partial x_j} = -\delta_{i3}g - \frac{1}{\rho_w}\frac{\partial p}{\partial x_i} + \nu \sum_{j=1}^{3} \frac{\partial^2 \overline{u_i}}{\partial x_j^2} - \sum_{j=1}^{3} \frac{\partial \overline{u_i' u_j'}}{\partial x_j} \tag{2.4}$$

Here, we have used the identities:

$$\begin{aligned} \overline{\overline{f_1}} &= \overline{f_1} \\ \overline{f_1'} &= 0 \\ \overline{f_1 f_2} &= \bar{f_1}\bar{f_2} + \overline{f_1' f_2'} \end{aligned} \tag{2.5}$$

for the random variables f_1 and f_2. The last term on the r.h.s. of Equation 2.4 is usually expressed as the Reynolds' stress:

$$\tau_{ij} = -\bar{\rho_w}\overline{(u_i' u_j')} \tag{2.6}$$

Subtracting from Equation 2.4 the mean flow, multiplying by u_i' and then time-averaging, one can obtain an expression for the Turbulent Kinetic Energy:

$$\frac{d}{dt}\text{TKE} = -\overline{u_i' u_j'}\frac{\partial \overline{u_i}}{\partial x_j} - \frac{\partial}{\partial x_j}\left[\frac{1}{\rho_w}\overline{u_j' p'} + \overline{u_j' u_i' u_i'} - \nu\frac{\partial}{\partial x_j}\text{TKE}\right] - \nu\overline{\left(\frac{\partial u_i'}{\partial x_j}\right)^2} - \frac{\overline{u_i'\rho_w'}}{\rho_w}g\delta_{i3} \tag{2.7}$$

with $\frac{d}{dt}$ denoting the material derivative[2]. TKE is defined as:

$$\text{TKE} = \frac{1}{2}\sum_{i=1}^{3}\overline{u_i'^2} \tag{2.8}$$

Assuming there are no spatial gradients in TKE and neglecting pressure correlations, one can simplify Equation 2.7 to:

$$\frac{\partial}{\partial t}\text{TKE} = -\overline{u_i' u_j'}\frac{\partial \overline{u_i}}{\partial x_j} - \nu\overline{\left(\frac{\partial u_i'}{\partial x_j}\right)^2} - \frac{\overline{u_i'\rho_w'}}{\rho_w}g\delta_{i3} \tag{2.9}$$

If we furthermore assume that the mean flow is in the x-direction ($u_2, u_3 = 0, u_1 = u_0$) and that the turbulence is homogeneous and isotropic, the following equation can be obtained:

$$\frac{\partial}{\partial t}\text{TKE} = P - \epsilon + B \tag{2.10}$$

---

[2] $\frac{d}{dt} = \frac{\partial}{\partial t} + \overline{u_j}\frac{\partial}{\partial x_j}$

where P is the production of TKE due to the mean flow, ϵ is the rate of dissipation of TKE due to friction and B the buoyancy flux. Here P, ϵ and B are defined as:

$$P = -\overline{u'_1 u'_3}\frac{\partial u_0}{\partial x_3}$$
$$\epsilon = 7.5\nu\overline{\left(\frac{\partial u'_1}{\partial x_3}\right)^2}$$
$$B = -\overline{\rho'_w u'_3}\frac{g}{\rho_w}$$

(2.11)

The factor of 7.5 applies to the special situation of statistically isotropic and homogeneous turbulence. It was first derived by Taylor [20]. P and ϵ are always positive, whereas B can change sign. Positive means destabilizing, while negative means destabilizing. Assuming that we have stationary conditions, one can find that:

$$\epsilon = P + B$$

(2.12)

The ratio $\frac{B}{\epsilon}$ is called the mixing efficiency, Γ. This ratio, often assumed to be 0.2, can be used to derive the vertical mixing coefficient [21]:

$$K_T = \Gamma\frac{\epsilon}{N^2}$$

(2.13)

with $N^2 = -\frac{g}{\rho_w}\frac{d\rho_w}{dx_3}$ being the buoyancy frequency.

2.1.1 Generation by wind

One of the mechanisms which creates TKE in a lake is forcing due to the wind (P). An important parameter which determines this forcing is the surface shear stress, τ, which is the force per unit area acting on the lake's surface:

$$\tau_{13} \equiv \tau = \rho_a C_{10} U_{10}^2 = \rho_a \overline{u'_{1,air} u'_{3,air}} = -\bar{\rho}_w \overline{u'_1 u'_3}$$

(2.14)

where ρ_a is the mean density of air, C_{10} is the wind drag coefficient and U_{10} the horizontal wind speed, both at 10 m height above the surface. Subsequently we can define the friction velocity as [22]:

$$u_* = \frac{\tau}{\bar{\rho}_w}$$

(2.15)

It can be shown that in a constant stress layer at the surface in steady state that:

$$\frac{\partial u_1}{\partial x_3} = -\frac{(u_*)^{1/2}}{\kappa x_3}$$

(2.16)

5

which is known as the 'Law of the Wall'. $\kappa = 0.41$ is the Von Kàrmàn constant and x_3 the depth. If we additionally assume that $B = 0$, one can obtain from Equations 2.12,2.15 and 2.16 that [23]:

$$\epsilon_{*s} = \frac{(u_*)^3}{\kappa x_3} \tag{2.17}$$

Hence, it is expected that in a surface mixed layer dominated by wind the dissipation decays with the inverse of the depth.

2.1.2 Generation by buoyancy

A second mechanism for creation of TKE is due to a positive buoyancy forcing at the surface (B_0), which causes convection. The buoyancy flux describes the production of potential energy due to density changes. A negative flux increases the potential energy by extracting kinetic energy from turbulent currents. So in a stably stratified column the flux is negative. But, if on the other hand B is positive, TKE is being produced. So a negative buoyancy flux is considered to be stabilizing, while a positive buoyancy flux is destabilizing. The surface buoyancy flux is due to the rate of change of density of a well mixed layer at the surface with a depth MLD. The MLD has been defined using a threshold method. It was defined as the depth where the density had increased by 0.1 kgm^{-3} relative to the surface density. The density was computed using the method of Chen and Millero [24]. Assuming the salinity to be zero, the surface buoyancy flux is defined as [19, p. 110]:

$$B_0 = \frac{\alpha g}{c_p \rho_w} Q_{tot} \tag{2.18}$$

with α being the thermal expansion coefficient, c_p the specific heat of water and Q_{tot} the total net heat flux at the surface. The total net heat flux is defined as:

$$Q_{tot} = Q_{SW} + Q_{LW} + Q_{LH} + Q_{SH} \tag{2.19}$$

where Q_{SW} is the incoming shortwave radiation, Q_{LW} the net longwave radiation, Q_{LH} the latent heat flux and Q_{SH} the sensible heat flux.

2.1.3 Monin-Obukhov length

Generally speaking, both of the above processes, convective mixing and mixing due to shear, play a role in the well mixed layer. If we assume that dissipation due to convective mixing is constant with depth ($\epsilon = B_0$), one can derive a length scale at which the dissipation due to convective mixing equals the dissipation due to shear. This length scale is called the Monin-Obukhov length:

$$L_{MO} = -\frac{u_*^3}{\kappa B_0} \tag{2.20}$$

At depths shallower than the Monin-Obukhov length wind-driven turbulence is expected to be dominant, while at greater depths than the Monin-Obukhov length turbulence due to convection is expected to be more important than wind-driven turbulence.

2.2 TKE dissipation

From the above it is clear that measurements of the TKE dissipation are the core of turbulence measurements. One of the ways to measure the dissipation relies on velocity gradient measurements with the help of airfoil shear probes [25]. This method was introduced by Osborn [26].

Kolmogorov was the first to derive the spectrum for turbulent velocity fluctuations. For this he assumed that the largest scales of turbulence are much larger than the dissipative scales (now called the Kolmogorov scale, $\eta = (\nu^3/\epsilon)^{1/4}$). He showed that the velocity spectrum must be proportional to $k^{-5/3}$, where k is the wavenumber, in the inertial subrange[3]. Based on work by Nasmyth [27], Oakey [28] derived an empirical spectrum, with which the rate of dissipation can be derived based on velocity fluctuations:

$$\epsilon = \nu \overline{\left(\frac{\partial u'}{\partial x_3}\right)^2} = \int_0^\infty \phi(k)dk \tag{2.21}$$

where $\phi(k)$ is called the Nasmyth Universal Spectrum, defined as [25]:

$$\phi(k) = \frac{8.05(k\eta)^{1/3}}{1 + (20.6k\eta)^{3.715}} \tag{2.22}$$

This spectrum will be used to determine the TKE dissipation.

2.3 MicroCTD Measurements

Since March 2017 a monitoring program has been established in Lake Garda [29]. In the light of this monitoring program high-resolution profiles of temperature, chlorophyll-a and velocity fluctuations have been obtained using a MicroCTD (Rockland Scientific International, Canada). A MicroCTD is a vertically free-falling turbulence and CTD profiler suitable for lakes. The instrument can be operated at depths upto 100 m. The instrument contains two shear probes, which measure velocity fluctuations, two FP07 thermistors with an accuracy of 0.001 $°C$ and a resolution of 5×10^{-5} $°C$ and a chlorophyll-a turbidty sensor and fluorometer (JFE-Advantech Sensors) with an accuracy of 1 ppb and a resolution of 0.01 ppb for the fluorometer. The turbidity sensor has an accuracy of upto 0.3 FTU and a resolution of 0.03 FTU. Furthermore, a conductivity sensor was mounted with an accuracy of 0.01 mS cm^{-1} and a resolution of 0.001 mS cm^{-1}. Finally, the mounted shear probes have an operating range of 0-10s^{-1} an accuracy of 5% and a resolution of $10^{-3}s^{-1}$. Based on depth measurements it was determined that the profiler descends at a speed of about 0.75 ms^{-1}. The sampling frequency for these sensors is

---

[3]The range of wavenumbers for which velocity fluctuations are not affected by viscosity.

512 Hz. This high sampling frequency results in a spatial resolution of approximately 1 mm.

2.3.1 Shear velocity

The MicroCTD comes with a specially developed MATLAB® library to preprocess the measured profiles. First of all, the measured profiles are despiked and band-pass filtered between 0.4-98 Hz. The resulting velocity fluctuations are Fourier transformed using a Cosine window with 50% overlapping segments [30] and a bin length of 0.75 m (1 s). The dissipation rate is determined from an ensemble average of several of these segments. To provide statistical robustness one dissipation bin was chosen to be 4 times the bin length of the Fourier transformed segments: 3 m (4 s). Hence, one dissipation estimate consisted of 7 Fourier segments. The dissipations bins have an overlap of 75% and this results in a dissipation estimate every 0.75 m. In order to obtain a dissipation estimate the sprectra are fitted to the Nasmyth Universal Spectrum as defined in Section 2.2. For more details about how the spectra are being fitted, see the Technical Notes by Rockland Scientific International Inc., especially Technical Note 28 [30] by Lueck and Technical Note 5 [31] by Lueck.

2.3.2 Thorpe Scale

An alternative measure of mixing is to identify density inversions in the water column using standard CTD-measurements. A density inversion may signify an overturning motion and this overturning motion results in mixing [32]. The associated vertical scale of these overturning motions is called the Thorpe scale (L_T) and is defined as:

$$L_T = (\bar{d^2})^{1/2} \tag{2.23}$$

where d is the displacement of water parcels in a measured potential density or temperature profile required to reorder the profile in such a way that it will be gravitationally stable. The bar here denotes an arithmetic mean. The Thorpe scale is known to be closely related to the Ozmidov length scale, sometimes referred to as the buoyancy scale. This scale is the maximum length over which an eddy could expand without losing its isotropy [33] or the overturning length scale at which the buoyancy forces balances the inertial forces. It is defined as:

$$L_{Oz} = \left(\frac{\epsilon}{N^3}\right)^{\frac{1}{2}} \tag{2.24}$$

It has been shown by Dillon [34] that the Ozmidov scale and the Thorpe scale are related by a factor of 0.8:

$$L_T \approx 0.8 L_{Oz} \tag{2.25}$$

In a fresh water lake like Lake Garda, the biggest potential density differences are due to temperature differences rather than differences in salinity. Therefore we will assume

that the potential temperature can be used as an indirect measure of the potential density. The potential temperature was deduced from the measured temperature profiles using the MATLAB® oceanography toolbox[4], which uses a polynomial to determine the adiabatic lapse rate and a Runge-Kutta fourth-order integration scheme [35].

Thorpe scales have been shown to give reasonable estimates of vertical mixing in regions with relatively high stratification and mixing rates [36][37]. In regimes where the mixing rates are low, instrument noise becomes a serious problem. This instrument noise might introduce spurious density inversions in the measured potential density profiles. This will result in an over-estimation of the Thorpe scale if these spurious overturns are treated as real overturns. Therefore a method has to be used to effectively eliminate the noise created by the instrument in such environments, while at the same time preserving the real overturns. A number of methods exist and one of these methods is a method proposed by Galbraith and Kelley [38]. They propose that a useful property to distinguish between real and spurious overturns might be a statistical measure called the "run length". This measure groups adjacent water parcels in a water column, which are moving in the same direction to obtain an

Figure 2.1: *A schematic sketch of a density inversion (black line) on a background density stratification (dashed line). The run length is three here, since three adjacent water parcels (black dots) have been moving in the same direction.*

adiabatically stable profile. The length of such a group of parcels moving in the same direction is called the "run length". An example is shown in Figure 2.1. They compared the root-mean-square run length for a series of density differences between the measured density profile and the reordered profile, called the Thorpe fluctuation series, with that of an expected distribution from a random series:

$$P(n) = 2^{-n} \tag{2.26}$$

where $P(n)$ is the chance for a run of length n.

It has been shown by Johnson and Garrett [39] that it is insufficient to neglect the background density stratification of an overturn and that the method by Galbraith and Kelley is too strict and likely to reject real overturns. Because of this Johnson and Garrett introduced an extension on the above method. This extension simulates noisy overturns on a background linear potential density profile. The noisy overturns are simulated as being normally distributed noise with an amplitude which is equal to the instrument's resolution limit. The run lengths and Thorpe scales of these simulated profiles can be
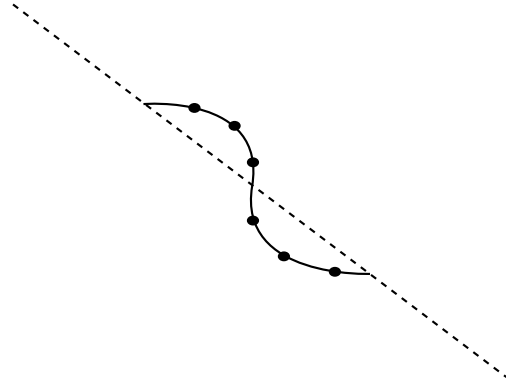
---

[4]see: http://mooring.ucsd.edu/software/matlab/doc/ocean/index.html

compared to the measured profiles to assess whether the found overturns in our profile are distinguishable from noise or not. The algorithm by Johnson and Garrett has been extended here to include non-linear profiles. To achieve this, every measured profile has been subsampled to 1 Hz using non-overlapping moving averages to obtain a "mean" profile and then interpolated to the original resolution. On top of this we simulated normally distributed noise with an amplitude of $\sigma_\theta = 5 \times 10^{-5}$ °C. This value is based on the resolution of the instrument, see also section 2.3. This simulation was carried out 100 times for each profile. For the calculation of the Thorpe scale we have only considered run lengths bigger than the run lengths expected from an expected distribution of a random series. Additionally, only profiles that had a rms run length and a Thorpe scale significantly bigger than those obtained from the simulations were considered to minimize the effect of noise. Significantly here means more than three standard deviations above the noise level obtained from simulations.

Chapter 3

Results

With the help of in-situ measurements vertical microstructure profiles have been obtained of temperature, chlorophyll-a and shear velocity fluctuations. These profiles can be used to derive turbulent characteristics like the Turbulent Kinetic Energy dissipation, ϵ, Vertical mixing coefficient (κ_T) and the Thorpe scale (L_T). These profiles have been obtained for a full seasonal cycle from March 2017 until March 2018. In addition to this, nearby meteorological data has been obtained during this period to assess the meteorological forcing on the lake.

3.1   Measurement Locations

Four different locations have been observed during the monitoring campaign (see Figure 3.1). One of them, called the Reference Station (RS) is located in the center of the narrow part of the lake, about 4 km from the northern edge. Towards the shores two different stations are located on opposite ends of the Reference Station, called the Western Station (WS) and the Eastern Station (ES). Together, these three stations form a cross section which is perpendicular to the lake's main axis, which is oriented in a northeast-southwest direction. The fourth station is located further to the south and is called the Limone Station (LS). In total 473 profiles have been taken in the period 8 March 2017 to 23 March 2018. At least three, but preferably five, profiles were taken on a single site before going to a next site, to make the results statistically more reliable.

3.2   Meteorological Data

Meteorological data was obtained from a nearby meteorological station in Limone Sul Garda (LW in Figure 3.1). The station is maintained by the Environmental Protection Agency of Region Lombardia (ARPA Lombardia)[1]. This station collects hourly data of air temperature, relative humidity and wind speed and direction, among other things. The station is located at an altitude of 75 m, which is 10 m higher than the altitude of the lake. The wind speed and direction were measured at a height of 16 m above the

---

[1]see: http://www.arpalombardia.it/siti/arpalombardia/meteo/previsionimeteo/
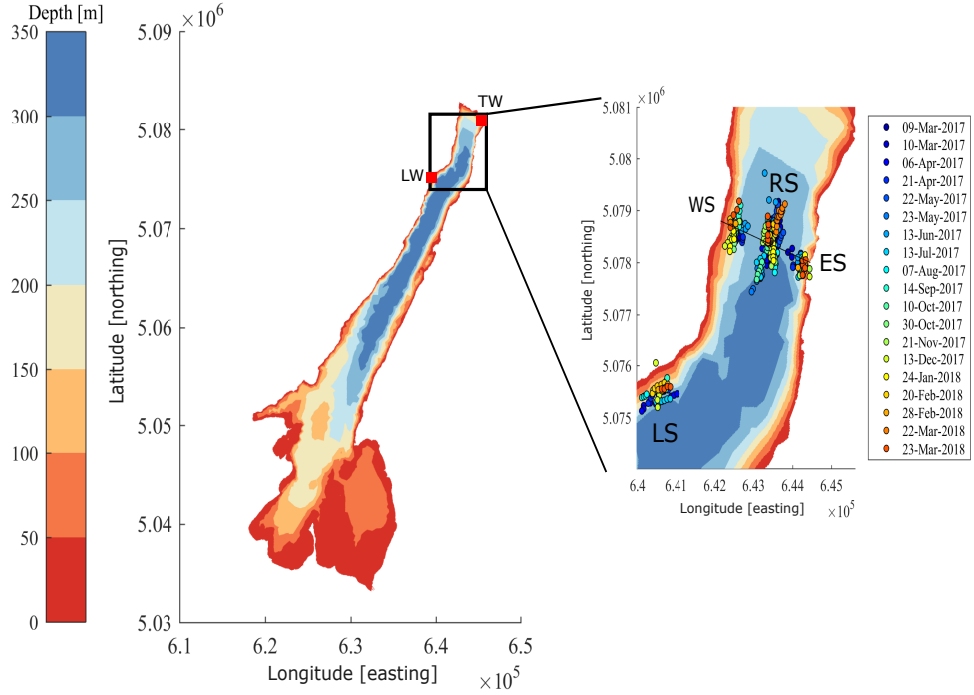meteolombardia/Pagine/default.aspx

Figure 3.1: *The locations where the measurements have been carried out. RS indicates the Reference Station, LS the Limone Station and ES and WS the Eastern and Western Station. The weather stations are indicated as red squares: LW for the station at Limone Sul Garda, TW for the one in Torbole.*

surface and the air temperature and relative humidity data were collected at a height of 1.7 m above the surface.

A different meteorological station is located around 10 km northeast of Limone Sul Garda in Torbole (TW in Figure 3.1). This station collects hourly data of incoming solar radiation. We assumed that the incoming solar radiation at Torbole is comparable to that of Limone Sul Garda.

The data thus obtained can be used to derive the net surface heat flux with the help of the Lake Heat Flux Analyzer [40], provided that there is data for the surface water temperature as well. The Lake Heat Flux Analyzer has been slightly adapted for the calculation of cloud cover. Cloud cover data was obtained from a meteorological station in Tremalzo located 1560 m above sea level to minimize the effect of mountains. The cloud cover was calculated as:

$$C_f = 1 - \frac{Q_{SW,obs}}{Q_{SW,clearsky}} \tag{3.1}$$

where C_f the cloud cover fraction, $Q_{SW,obs}$ the observed incoming solar radiation and $Q_{SW,clearsky}$ the incoming solar radiation in clear sky conditions.

In order to obtain a daily resolution of the net surface heat flux we have used the air2water model [41], which simulates the surface water temperature from air temperatures. The input for the model was the air temperature data from the Limone Sul Garda weather station and lake surface temperature data from APPA, the Environmental Protection Agency of the province of Trento. This data is collected on a monthly basis at the same location as where the Reference Station on the transect is located. For model calibration the years 2012-2017 have been used. The total net heat flux was used to determine the surface buoyancy flux and the Monin-Obukhov length.

3.3 Meteorological Forcing

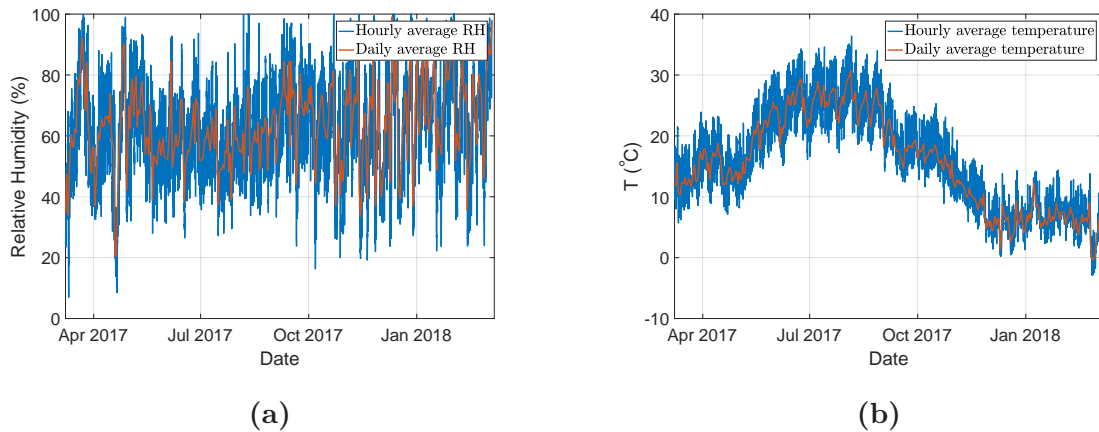### 3.3.1 Temperature, Relative Humidity & Wind conditions

Figure 3.2: *(a): Hourly and daily average relative humidity in percentage in the period 7 March 2017 to 7 March 2018.(b): Hourly and daily average air temperature in degrees Celsius in the period 7 March 2017 to 7 March 2018.*

In Figure 3.2 the temperature and relative humidity evolution over a period of 1 year is shown. The relative humidity (Figure 3.2a) turned out to be highly variable but was about $(62 \pm 46)\%$ on average over the whole year. A clear seasonal cycle cannot be distinguished. However, the variability seems to be decreasing in the summer months (JJA) compared to the rest of the year. In the other months the variability was bigger and it was also in those months that relatively high ($> 90\%$) and low ($< 30\%$) values were found the most.

A much clearer signal was obtained from the air temperature (Figure 3.2b). The temperature shows a clear seasonal signal with a maximum in the summer months (JJA) and a minimum in the winter months (DJF). In the summer months the mean temperature was $25 \pm 4°C$, while in the winter months it was $6 \pm 3°C$. Hence there is a temperature difference of $19 \pm 5°C$ between the summer and winter months.

Figures 3.3 and 3.4 show the wind conditions as they were found on the lake during the year. If we look at the measured wind speeds (Figure 3.3) we notice that it varies wildly over the year from no wind at all to a maximum wind speed of 12.9 ms^{-1}, measured on

September 12. The mean wind speed was determined to be $2.6 \pm 1.9\ ms^{-1}$ over the whole year. In general a seasonal cycle cannot be distinguished from this data. However there have been some noticeable wind events during the year. Two of these events, namely those on April 19 and August 6 happened to be events which preceded measurement days. The event on August 6 is interesting since it had the third highest wind speed measured over the year ($12.6\ ms^{-1}$), even though on a daily scale it does not seem to be particularly spectacular. On the other hand, the April 19 event had lower wind speeds, but it lasted almost two days.

As can be seen in Figures 3.4a and 3.4b, the wind has two clear preferential directions, namely a direction around 190° and 45°. A third, less clear preferential direction can be distinguished around 260°. The associated wind speeds are very low compared to the other two directions, though. Over the year it turned out there is a weak daily cycle as well. A discussion of this can be found in Appendix A.1.
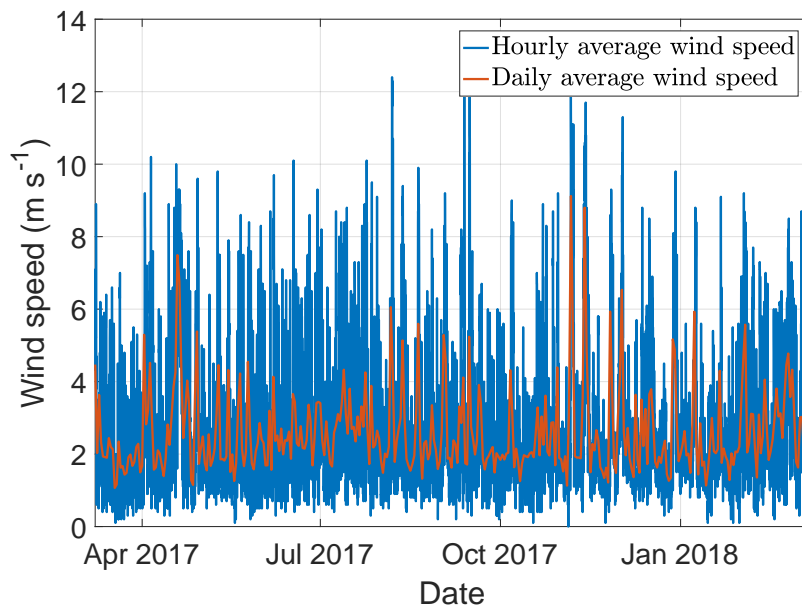

Figure 3.3: *Hourly and daily average wind speed in ms^{-1} in the period 7 March 2017 to 7 March 2018.*
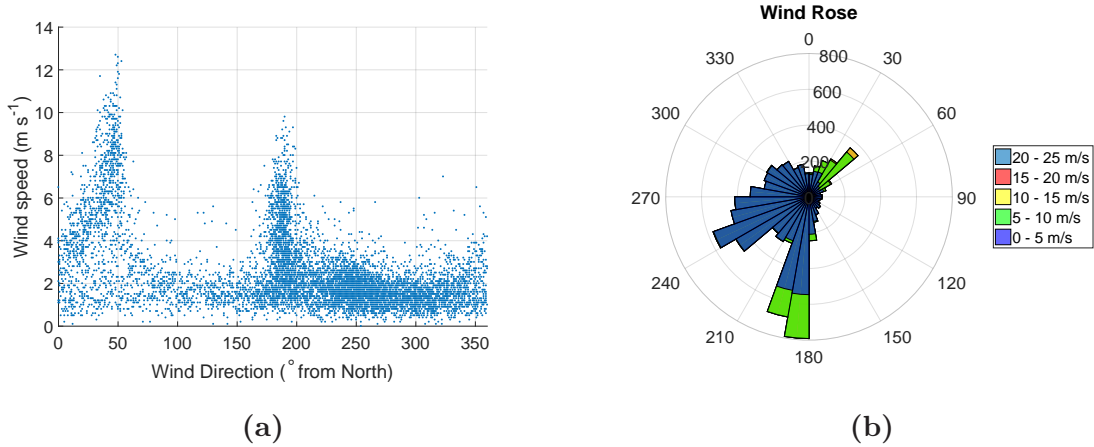
Figure 3.4: *(a): Scatter plot of wind direction and wind speed. Every dot represents an hourly mean wind speed. (b): A windrose showing the dominant wind directions. The colour indicates the measured wind speed, while the length shows direction and amount of data points collected in the specific bin (radial axis).*

3.3.2 Net radiation and buoyancy flux

Figure 3.5a shows the incoming short-wave radiation as it was measured at the Torbole weather station. The short-wave radiation has a seasonal cycle as would be expected. The maximum daily average short-wave radiation was reached on June 18 with a value of almost 330 Wm^{-2}, while the minimum was reached on December 27 with a value of 0 Wm^{-2}. The computed daily average values of the net surface heat flux are shown in Figure 3.5b.
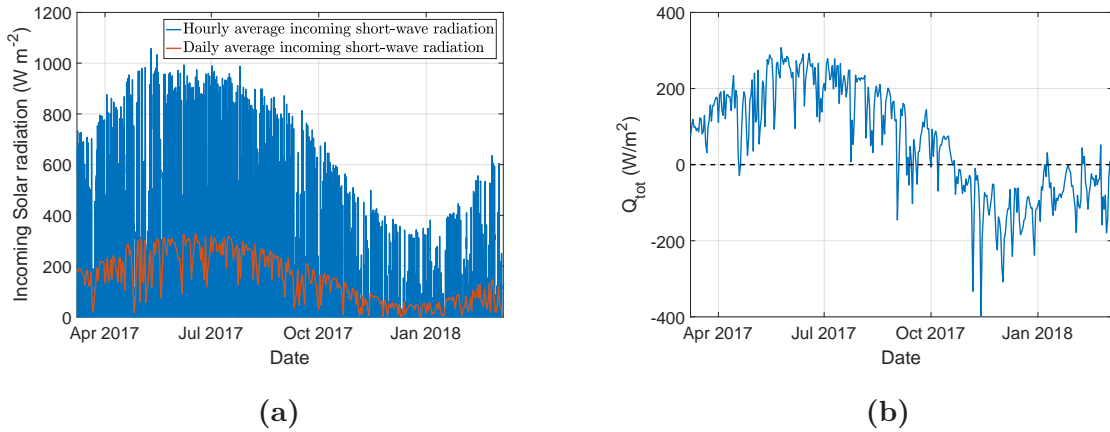

Figure 3.5: *(a): Measured average hourly and daily solar radiation at the Torbole weather station. (b): The obtained daily average net surface heat flux as calculated with the help of the Lake Heat Flux Analyzer [40].*

During the months March and April 2017 the net surface heat flux was mainly positive, although there was a day with a negative surface heat flux on April 19 of -29 Wm^{-2} on average. The next day with an average net heat flux below zero was registered on September 2 with an average of -145 Wm^{-2}. A transition period is started in the begin-
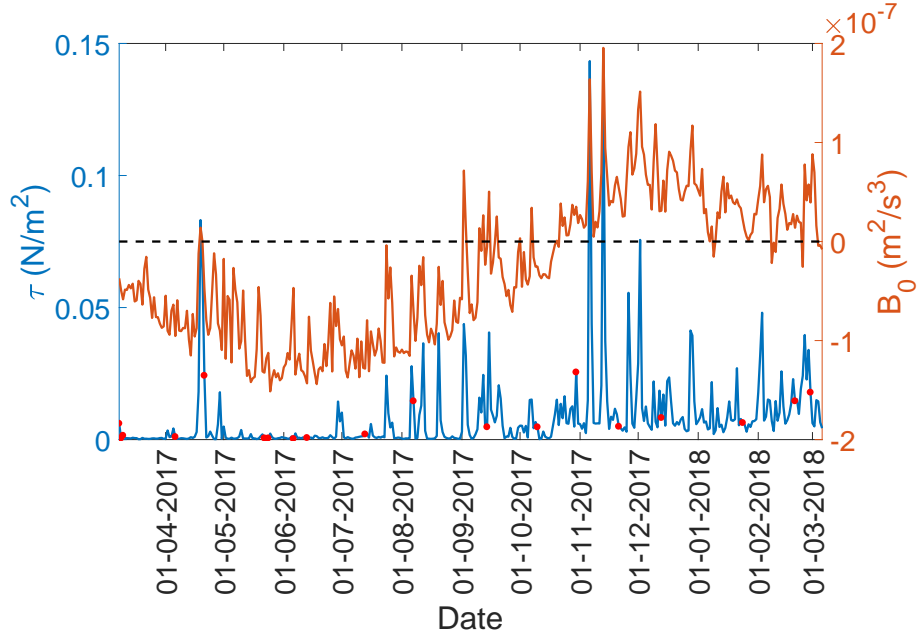
15

Figure 3.6: *The daily average wind stress, τ, in Nm^{-2} is indicated in blue and the daily average surface buoyancy flux, B_0, in m^2s^{-3}, is indicated in orange for the period 7 March 2017 to 7 March 2018. the dashed line indicates a neutral buoyancy flux (0 m^2s^{-3}). The red dots indicate measurement days.*

ning of September which lasted until October 21. This was a period where both negative and positive net heat fluxes were being registered. October 21, 2017 was the last day that a net positive heat flux was registered until it would happen again for the first time in 2018 on January 9.

Since the surface buoyancy flux is directly depending on the total net surface heat flux, the seasonal cycle described above is clearly visible in the surface buoyancy flux as well. The daily average surface buoyancy flux is shown in Figure 3.6 together with the daily average wind stress forcing τ. In the summer and spring of 2017 the surface buoyancy flux was mostly negative, which means that it was stabilizing and thus repressing turbulence. An interesting exception here was the period at the end of April. Two of these days, April 19 and 20, are also associated with a wind event. On these days the wind stress was 0.08 Nm^{-2}, which is about 10-100 times higher than other days during the spring. During the months September and October there is a transition period where the surface buoyancy flux changes from positive to negative and vice versa. From October 21 onwards the buoyancy flux stays destabilizing (i.e. positive) until January 9 in 2018. The surface buoyancy flux thus ranges from -1.5×10^{-7} to 2×10^{-7} m^2s^{-3} throughout the year, with negative values being found mostly between April and September and positive values being found during the period October till March. The transition periods are in September/October and February/March.

When we compare the surface buoyancy flux B_0 with the wind stress forcing τ a pattern seems to emerge. Peaks in the surface buoyancy flux seem to be associated with peaks in the wind stress. The most clear examples are April 19 and 20, as discussed but
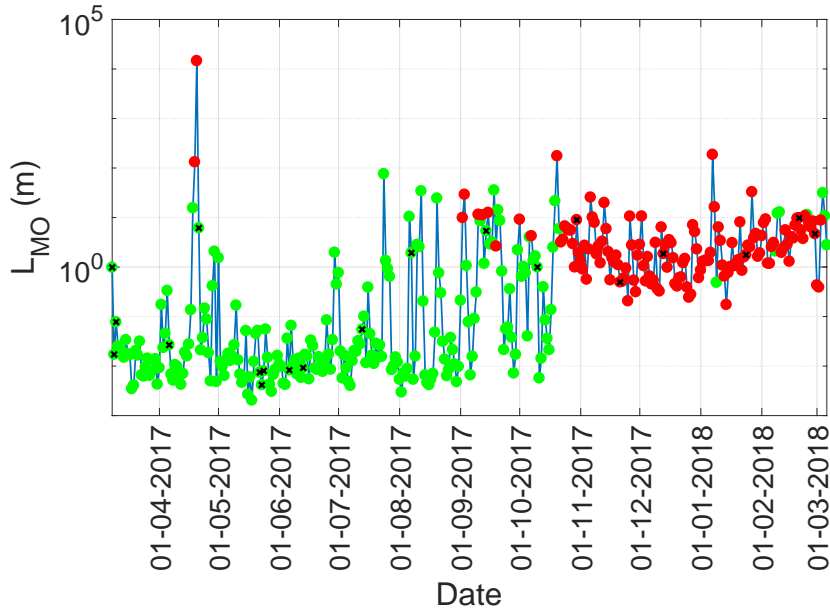
Figure 3.7: *The daily average Monin-Obukhov scale (L_{MO}) over the period 7 March 2017 to 7 March 2018. Green means stabilizing, red means destabilizing. The black crosses indicate the measurement days.*

also November 6 and 13, which have the highest wind stress measured over the year. The wind stress increases suddenly in October.

3.3.3 The Monin-Obukhov Length

With the help of the wind stress and the buoyancy flux the Monin-Obukhov length can be determined. The result is shown in Figure 3.7. The Monin-Obukhov length is ranging over almost 7 orders of magnitude from as small as 2×10^{-3} m to as big as 1.4×10^4 m. Interestingly there is a clear transition in the magnitude of the Monin-Obukhov scales in October. From March 2017 until September 2017 the Monin-Obukhov scale is relatively small, certainly upto July. However, during September and October the scale increases by almost 2 orders of magnitude to unity length scale and also transitions from a stabilizing regime to a destabilizing regime. This thus means that the buoyancy flux is not suppressing the production of TKE anymore, but starts producing TKE, instead.

3.4 Reference Location

3.4.1 Temperature and Chlorophyll-*a* evolution

In Figure 3.8a the temperature evolution at the Reference Station is shown for various isobaths. The measurements made on August 7 turned out to be part of an anomalous event, which will be discussed later. For this reason this measurement has been left out
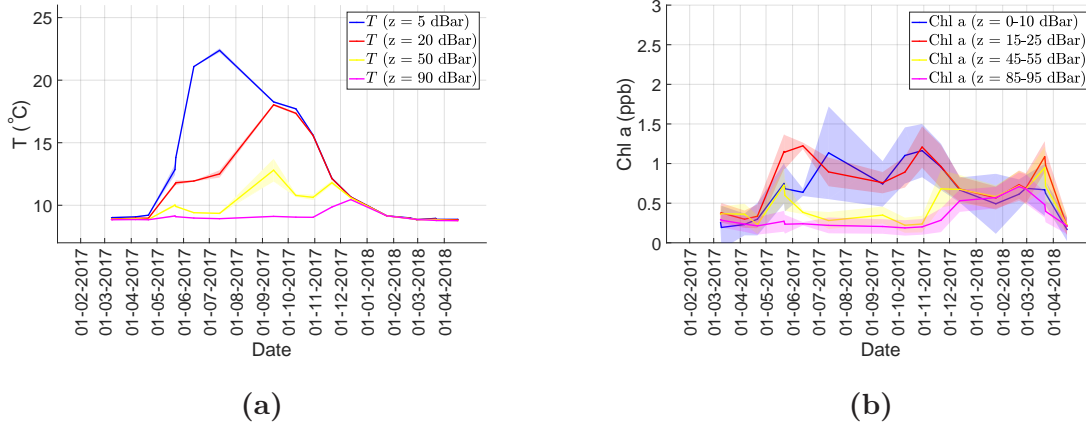
Figure 3.8: *(a) Temperature and (b) Chl-a evolution at Reference Station. The shaded areas indicate 95% confidence intervals. The colours, blue, red, yellow and pink indicate the depths 5, 20, 50 and 90 dBar depths, respectively. For chlorophyll-a a mean was taken over 10 dBar centred around these depths.*

from Figures 3.8a and 3.8b.

The temperature increased at all depths between April and the end of May. At 5 dBar depth the temperature was increasing until July and reaches a maximum temperature of 22.38 ± 0.09 °C. For greater depths the maximum temperature was not reached in July, but seems to be lagged. At depths of 20 dBar and 50 dBar the maximum temperature was reached in September with temperatures of 18.03 ± 0.04 °C and 12.8 ± 0.5 °C, respectively. At a depth of 50 dBar a second, but smaller, peak (11.81 ± 0.09 °C) was being observed in November. At an even greater depth of 90 dBar the maximum temperature was reached in December with a temperature of 10.45 ± 0.01 °C. The water column was completely mixed on January 24 with a temperature of 9.152 ± 0.001 °C and it would keep cooling down until March 23 with a temperature of 8.779 ± 0.001 °C being reached at 90 m depth that day.

A slightly different approach has been taken for the Chl-*a* evolution. Here we have taken the mean value of the Chl-*a* over a range of depths of 10 dBar, centred around 5, 20, 50 and 90 m. The results are shown in Figure 3.8b. A different pattern is observed when compared to the temperature evolution. The Chl-*a* concentrations were rising sharply at the depths up to 50 dBar during April and May. The biggest increase and biggest concentration were observed around 20 dBar with a maximum concentration of 1.224 ± 0.021 ppb being reached on June, 13. The concentrations at the surface (5 dBar) were significantly lower on this day with a concentration of 0.637 ± 0.024 ppb. In fact, the surface concentration went down compared to the previous month on May 22, when a maximum was observed, albeit not significantly. A maximum was also observed at 50 dBar (0.73 ± 0.12 ppb) at that day. From June onwards the Chl-*a* concentrations decrease (20 and 50 dBar) in July or do not change significantly (90 dBar). A peak concentration was observed at a depth of 5 dBar in July. Throughout the summer and early autumn there was little significant change in the concentrations. This changes in October. In October a peak in concentrations was observed at 5 dBar and 20 dBar of 1.16 ± 0.17 ppb and 1.21 ± 0.13 ppb, while in the preceding month the concentrations were 0.74 ± 0.15 ppb
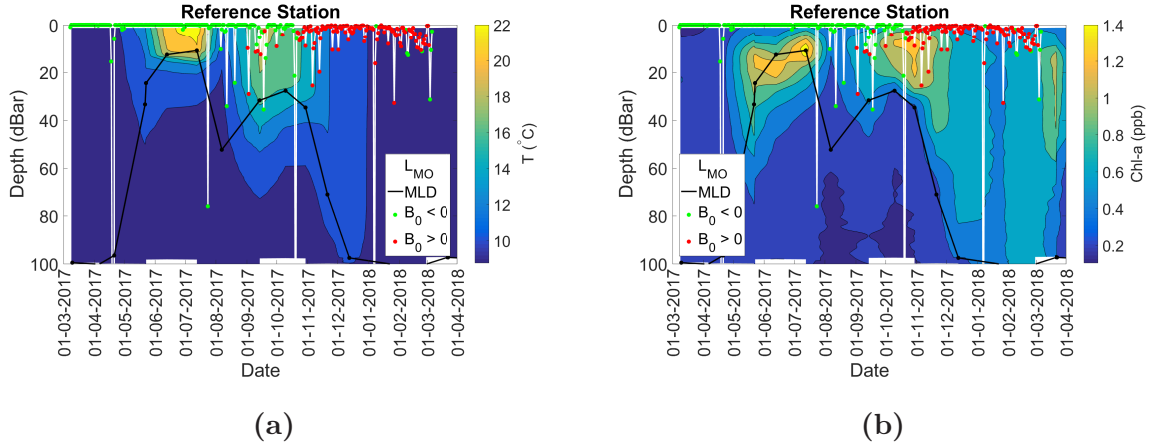
18

Figure 3.9: *(a) Temperature and (b) Chl-a contour evolution at Reference Station. The contour lines indicate intervals of 2°C for the left figure and 0.2 ppb for the right figure. The black line indicates the Mixed Layer Depth, with the black dots showing the individual measurements. The white lines indicate the Monin-Obukhov length (L_{MO}). Here, a green dot indicates that the buoyancy flux was stabilizing, while a red dot indicates destabilizing.*

and 0.76 ± 0.07 ppb, respectively. In November an increase was measured at 50 dBar after which the profile became homogeneously mixed in the following months.

3.4.2   Mixed Layer Depth and Monin-Obukhov length

Figure 3.9 shows contour plots for both temperature and Chl-*a*. The contour plots in this and subsequent sections were made by using linear interpolation between measurement days. Also shown are the Mixed Layer Depth and the Monin-Obukhov length. During the month May the stratification quickly increased and this was also found in the MLD which became quickly shallower from about 96.5 dBar on April 21 to 24 dBar on May 23. During June and July the the MLD became even shallower with a minimum depth being reached in July of 11 m, which was also when the temperature reached its maximum. In August the MLD deepened temporarily to 52 dBar, only to climb up again during September and October, when the lake was stratifying again with a second minimum being reached on October 10 of 28 dBar. From the end of October until the beginning of December the MLD deepened very fast and reached a maximum of about 100 dBar in the winter.

When we compare the MLD with the Monin-Obukhov length (L_{MO}) we notice that there are only a few occasions where L_{MO} exceeded the MLD at the reference station. This happened for the days April 19, July 24, September 18, October 20 and January 7. Of these only April 19, October 20 and January 7 were destabilizing. Above L_{MO} mixing due to shear is expected to be dominant. Hence, most of the time the mixing in most parts of the MLD, namely at depths below L_{MO}, is dominated by buoyancy and not by wind, but occasionally wind can play an important role in the production of TKE in the mixed layer.

In Figure 3.9b we notice that the Chlorophyll-*a* was increasing during May mainly above the MLD, but during June a maximum concentration was found just below the
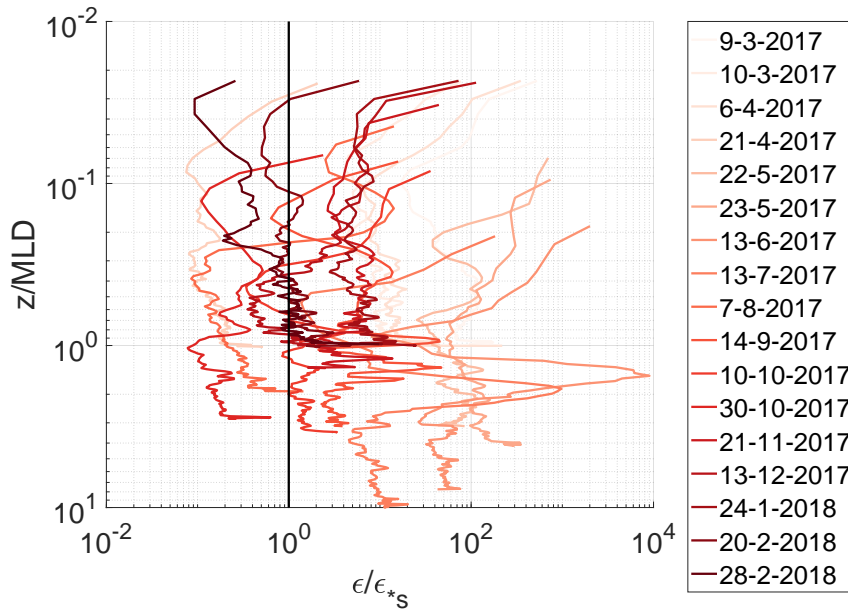
Figure 3.10: *Measurements of TKE dissipation scaled with Law of the wall (ϵ_{*s}) at Reference Station. the black vertical line indicates an ideal scaling. The color scheme indicates time.*

MLD and in July the maximum concentration was found at the depth of MLD. In subsequent months most of the Chlorophyll-*a* was found above the MLD and the MLD itself was mainly following the 0.4 ppb contour from October onwards. During November and December, the concentration is lowered at the surface (above 40 dBar) and increased in the lower layers. A second increase in the chlorophyll-*a* was found during the transition from a stabilizing to a destabilizing L_{MO}.

3.4.3 Dissipation and Vertical Mixing

Figure 3.10 shows a scaling of TKE dissipation with the Law of the Wall. The depth is scaled with the Mixed Layer depth. The black line indicates a perfect scaling with the Law of the wall. As can be seen from this Figure, most of the time the found dissipation is a much higher throughout the column than what could be expected from the wind only. For some days, though, the found dissipation was actually lower, namely for 21 April, 30 October and August 7.

Figure 3.11 shows a contour plot of the measurements for dissipation and the vertical mixing coefficient. On top of it, there is once again the MLD in black and the L_{MO} in white. From this Figure there is no clear seasonal variability in either the dissipation[2] or the vertical mixing coefficient. However, there are some features worth noticing. First of all, the dissipation and vertical mixing close to the surface were significantly higher than at a greater depths of 50 dBar and below. The values which were measured at the surface can be upto a factor of 100 higher than the values at a depth of 50 dBar. The

---

[2]It must be noted that ϵ is lognormally distributed [42]. Therefore the uncertainty can be upto an order of magnitude for individual measurements.
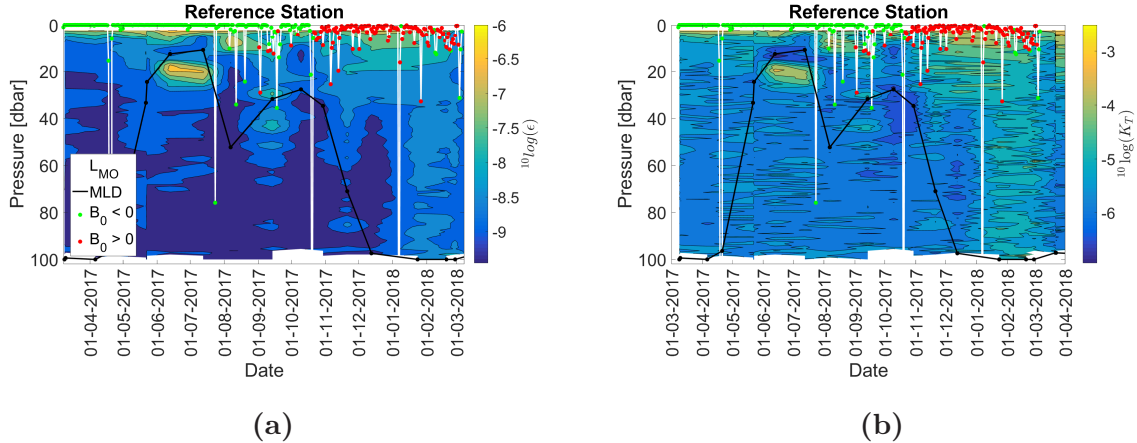
Figure 3.11: *Time evolution of **(a)** dissipation and **(b)** Vertical mixing coefficient contours at the Reference Station. The contour intervals are 0.5 **(a)** and 1 **(b)**, respectively. The black line indicates the Mixed Layer Depth, with the black dots showing the individual measurements. The white lines indicate the Monin-Obukhov length (L_{MO}). Here, a green dot indicates that the buoyancy flux was stabilizing, while a red dot indicates destabilizing. The contour plots were made by using linear interpolation between measurement days.*

values range from about 10^{-7} m^2s^{-3} at the surface to 10^{-9} m^2s^{-3} at 50 dBar and below. Secondly, during June and July there was a large jump in the measurements, just below the MLD. The dissipation and vertical mixing increased by a factor of 100. The reason for this is unknown, but it was present at all stations for all profiles during these two measurement days, which were about a month apart in time. At the MLD there was a minimum in the vertical mixing of $10^{-6.9}$ m^2s^{-1}, while just below it at about 20 dBar it was $10^{-3.5}$ m^2s^{-1}. Thirdly, in the period December to March the dissipation is increasing at all depths below 40 dBar. The dissipation in this period rose from 10^{-9} to 10^{-8} m^2s^{-3}.

3.4.4 Thorpe Scales

In figure 3.12 the root-mean square run length and the normalized Thorpe scale (L_T/H, $H = 100$ m) are compared to simulations with random noise as explained in section 2.3.2 for the Reference Station. Figure 3.12a shows us clearly that the measured run lengths in our profiles are generally much higher than those obtained from our simulations. Only 2 profiles, indicated in red, were found to have run lengths slightly below what is expected from random noise; hence they were not considered. The obtained Thorpe scales (Figure 3.12b) show more profiles that were rejected. 20 profiles were rejected based on the fact that they had a L_T indistinguishable from noise. So in total of the 424 profiles that were taken at the reference station, 22 were rejected, which is 5.2% of the total.

In order to distinguish whether there is any seasonal change in L_T at the reference station, all profiles have been categorized in which season they were taken. The seasons are defined as follows: December, January and February count as winter (abbreviated as DJF). March, April and May are considered to be the spring months (MAM). June, July and August (JJA) are the summer months, while September, October and November is
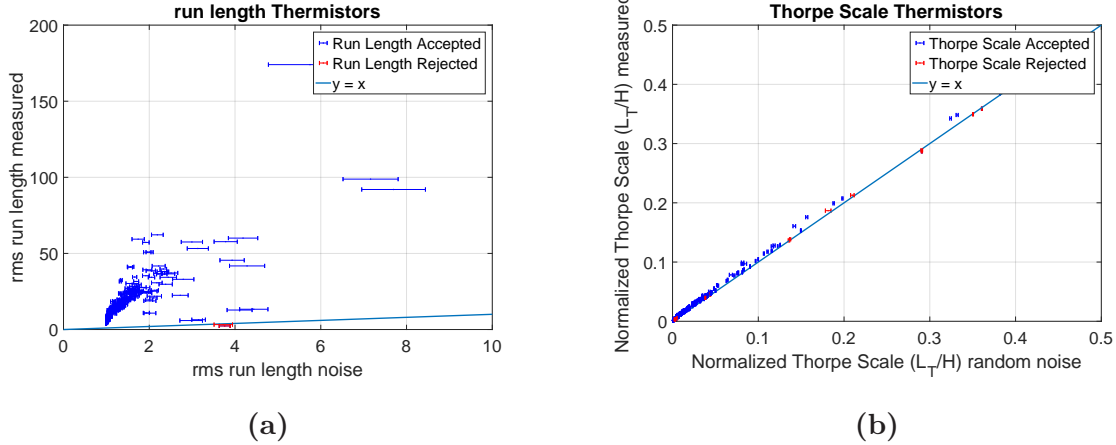
Figure 3.12: *(a): Comparison noise run length versus measured run length (b): Comparison Thorpe length from noise versus the measured normalized Thorpe length, with $H = 100$ m, the normalization constant. The blue solid lines indicate the line $y = x$. Profiles found below this line or less than three standard deviations away were considered indistinguishable from noise. Rejected profiles are indicated in red; accepted profiles are blue.*

considered to be the autumn. The results are shown in a stacked histogram in Figure 3.13.

Clearly, most of the profiles were taken during the spring (indicated in yellow). 238 of the profiles were taken in these months. Only 4 of the profiles were rejected in this period (1.7%). For the summer and the fall there are 48 and 74 profiles, respectively. 5 and 2 profiles were rejected, amounting to 10.4% and 2.7% being rejected. In the winter 11 out of 64 profiles were rejected in total, which is more than 17%.

Overall, a clear peak is distinguished between 0.1 and 0.2 m. 39.8% of all the measured values fall in this range. 86.6% of the profiles had a Thorpe length of less than 0.4 m. However, when sorted to season a different pattern appears. During the spring and the autumn almost all values lay in the region 0 to 0.4 m and have a peak between 0.1 and 0.2 m. The mean values were found to be 0.22 ± 0.12 m and 0.16 ± 0.08 m, respectively. In the summer even lower values were found and all values were found to be lower than 0.2 m. The mean was 0.106 ± 0.019 m. A clear peak cannot be distinguished. But, during the winter the values are much more spread out. In the winter the mean value was found to be 0.9 ± 2 m. The high uncertainty here comes from the fact that two profiles were found to have a L_T of more than 10 m. If we would leave these out the mean would be 0.53 ± 0.25 m.
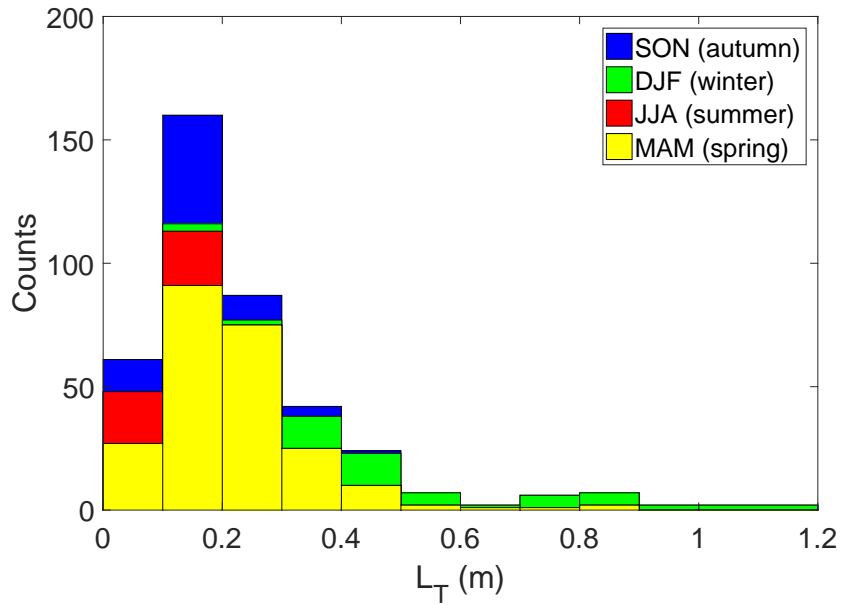
Figure 3.13: *Stacked histogram of the measured Thorpe lengths (L_T) divided per season: blue (autumn), green (winter), red (summer) and yellow (spring).*

3.5 East-West Anomalies

3.5.1 Lateral variability

The wind on Lake Garda is most of the time along the main axis and is rather predictable. A theoretical study by Toffolon [43] has shown that a wind-driven steady flow can develop in a closed basin with an elongated shape due to the Coriolis effect. This flow contains a secondary closed circulation, and, when lateral boundaries are present can cause significant up- and downwelling at the boundaries.

When a relatively strong wind is blowing over such a closed basin along its main axis, an Ekman transport mechanism may develop. A net transport of water will occur in a direction 90° to the right of the wind direction. This will cause a downwelling motion at the right side of the basin and an upwelling motion at the left side of the basin. A schematic sketch is presented in Figure 3.14.
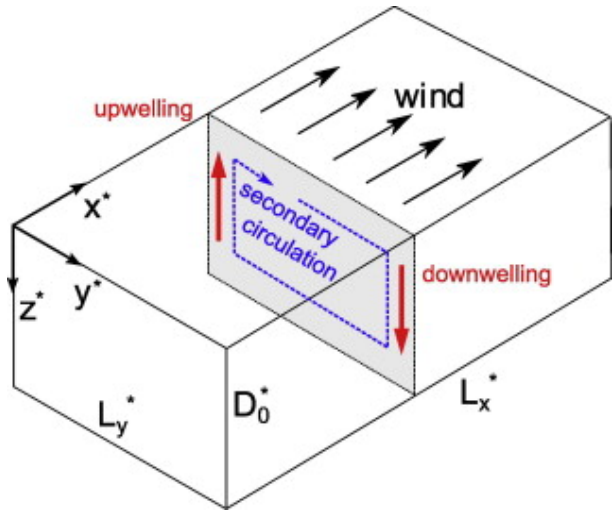

Figure 3.14: *A visual representation of an idealized version of the secondary circulation. Sketch taken from Toffolon [43].*

In order to assess whether anomalies were significant we defined the relative anomalies

as follows:

$$\frac{\overline{X_{StationY}} - \overline{X_{Ref}}}{\sigma_{Y+Ref}} \qquad (3.2)$$

where $\overline{X_{stationY}}$ is the mean of variable X^3 at station Y[4] and $\overline{X_{Ref}}$ the mean at the Reference Station. σ_{Y+Ref} is the combined standard deviation of the Reference station and station Y, defined as:

$$\sigma_{Y+Ref} = \sqrt{\sigma_{X,Ref}^2 + \sigma_{X,Y}^2} \qquad (3.3)$$

with $\sigma_{X,Ref}$ and $\sigma_{X,Y}$ the standard deviations for variable X at locations Reference Station and Station Y, respectively. The reason for this is to make the comparison as fair as possible for the different seasons as possible. For example, temperature variations are much bigger during summer than during winter and would therefore be much more pronounced if there would be no proper scaling. More than two standard deviations from the values found at the Reference Station is considered to be significant. The relative anomalies with explanatory text for temperature and chlorophyll-*a* can be found in Appendix A.2 and A.3, respectively. Graphs for the absolute anomalies can be found in Appendix A.4.

3.5.2 TKE Dissipation anomalies

In Figure 3.15 the TKE dissipation anomalies for the different stations (Western Station, Eastern Station and Limone Station) with respect to the Reference Station are shown. The contours in Figures 3.15a, 3.15c and 3.15b indicate levels of significant deviation. On top of it, there is once again the MLD in black and the L_{MO} in white. This time the MLD is associated with the specific station being considered. There are a few things that deserve attention.

On the 21st of April there was a significant event happening at the Eastern station, where almost the whole water column experienced significantly more TKE dissipation than the Western and Limone station. Also, we notice that during this moment there was a significant increase in the Monin-Obukhov length, which extended down below the Mixed Layer Depth. Secondly, we find patches of significant increases during December at all stations, but when we take a look at the dissipation at the Reference Station, we notice that it did not experience enhanced TKE dissipation. The most significant change was measured at Limone Station, with a few patches that are even more than 4 standard deviations away from the values found at the Reference Station.

The western part of the basin (Limone Station and Western Station) experienced a minimum in their MLD, with MLD's found to be only 7.1 dBar and 4.8 dBar for Limone Station and Western Station, respectively, on August 7. This is a contrast between the Eastern Station and Referene Station which experienced a local maximum of 53.6 and 52.4 dBar, respectively. Interestingly, an increased amount of TKE dissipation was found

---

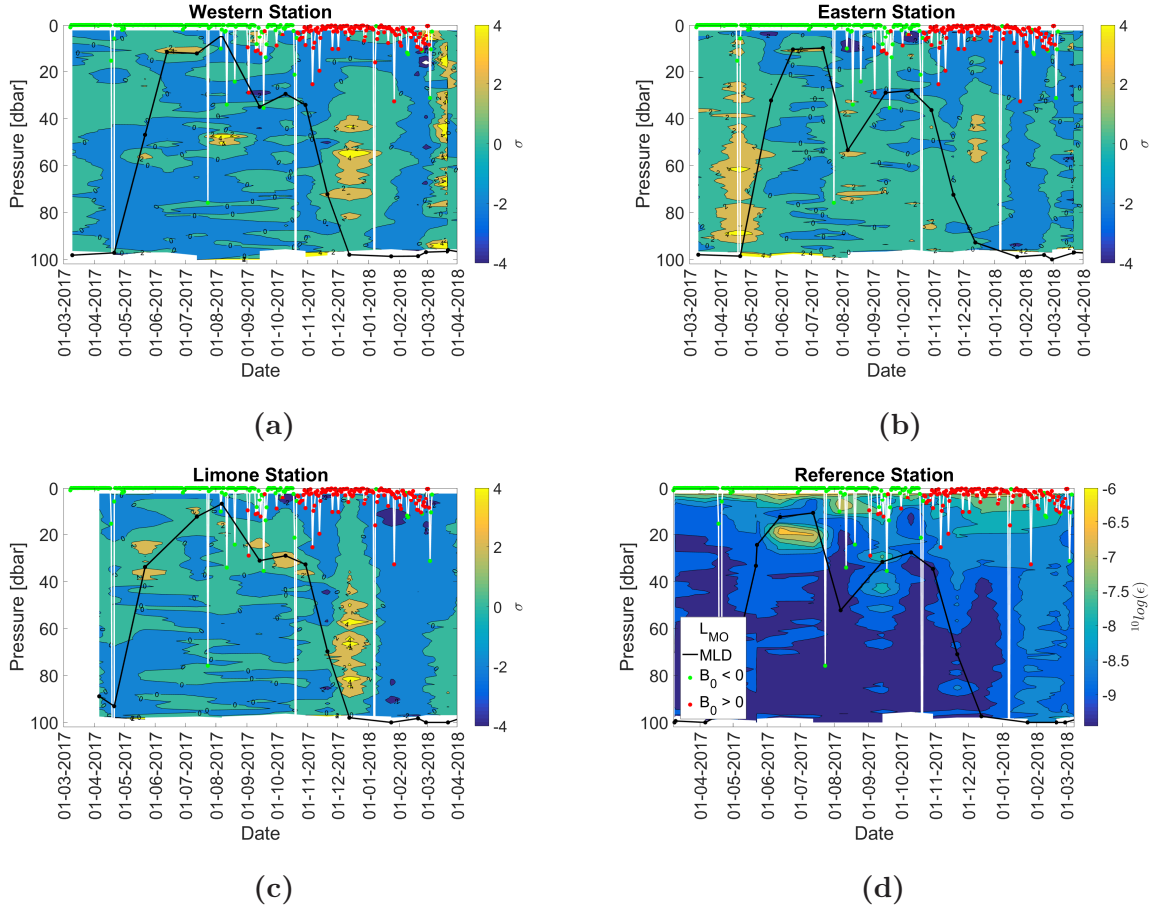[3]Chl-*a*, T or ϵ.
[4]Limone, East or West.

Figure 3.15: *Relative anomalies of TKE dissipation in terms of standard deviations, σ, for the stations: **(a)** West, **(b)** East and **(c)** Limone. The contour intervals are two standard deviations. Figure **(d)** shows the TKE dissipation in $^{10}\log(\epsilon)$ at the Reference station. The black line indicates the Mixed Layer Depth, with the black dots showing the individual measurements. The white lines indicate the Monin-Obukhov length (L_{MO}). Here, a green dot indicates that the buoyancy flux was stabilizing, while a red dot indicates destabilizing. The contour plots were made by using linear interpolation between measurement days.*

at the Eastern Station, although not significantly, at deeper layers below 20 dBar and a significant decrease in TKE dissipation at a depth of 10 dBar. A significant decrease in TKE dissipation was also found during October at the Limone Station and Eastern Station.

Chapter 4

Discussion

4.1 Meteorological Forcing

The air temperature, the incoming solar radiation and the total net heat flux show a clear seasonal cycle (Figures 3.2b, 3.5) as opposed to the relative humidity and the wind speed (Figures 3.2a and 3.3). These variables seem to be more event-based.

From Figures 3.4a and 3.4b it is clear that there are three preferential directions for the wind. From the west and south-southwest and northeast. These two last directions have to do with topography, since this part of the lake is rather narrow and is being surrounded by mountains. Therefore the wind on the lake is mainly along the lake's main axis northeast - southwest.

4.2 Atmospheric Stability

The net surface heat flux (Figure 3.5b) was mainly positive during March and April 2017, except for April 19, which was an event associated with strong winds. During the summer the net heat flux was positive. A transition period started on September 2 and ended on October 21 where alternating days of positive and negative heat fluxes were being registered. From October 21 onwards the net heat flux was negative until January 9, 2018.

The days of October 16 to October 22, marked a special point in the seasonal cycle. On this day a few things happened. First of all, as a result of the negative net heat flux, the buoyancy flux became destabilizing instead of stabilizing. Hence Turbulent Kinetic due to buoyancy was produced from that point on, instead of converted to potential energy (Figure 3.6). Also, the Monin-Obukhov length (L_{MO}) increased by a factor 24 in the period October 17 to October 22, with a Monin-Obukhov length of 175 m being reached on October 20 while a positive buoyancy flux was being measured (Figure 3.7). The sudden increase was due to an increase of the shear stress and thus an increase of the friction velocity u_*. The reason for the increase, however, was more fundamental. In Figure 4.1 the daily water temperature from the air2water model [41] and the daily air temperature are shown. Before October 18 the water temperature was most of the time lower than the air temperature. However, this changed after October 18. The water temperature became higher than the air temperature and only two days until January 9
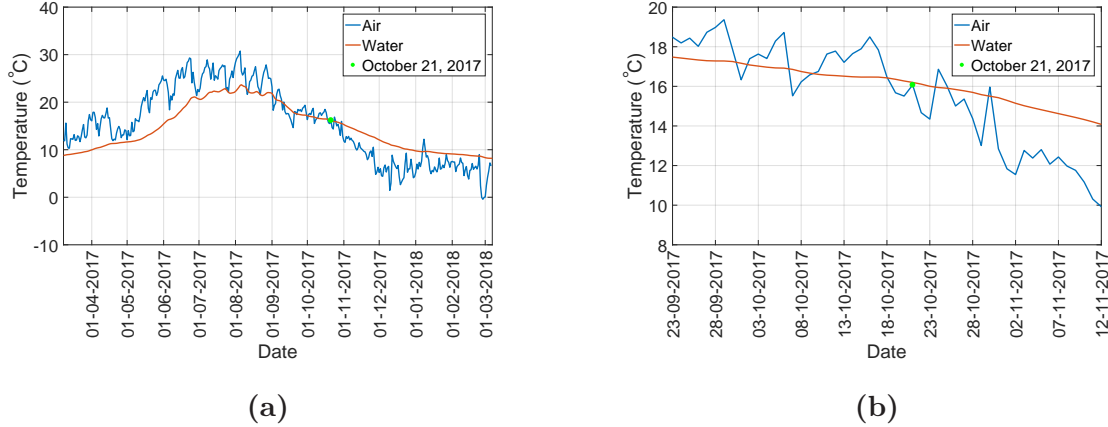
Figure 4.1: *(a): The daily air and water temperature evolution between March 2017 and March 2018. The green dot shows the transition point on October 21. (b): Same as (a), but zoomed in.*

had a higher daily average air than water temperature, namely October 24 and October 30. When the water temperature became higher than the air temperature, the air started to get heated from below and this resulted in the development of an unstable boundary layer in the atmosphere **and** in the water. This in turn increased the turbulent momentum flux, resulting in a higher wind stress.

The first algal bloom occurred in May and June. The beginning of the transition period marked the onset of a second algal bloom, which occurred during the months of September and October. This is shown in Figure 4.2 for the Reference Station. A clear increase above the MLD was observed throughout the period. Possibly the transition period plays an important role here, since generally, the circumstances are rather spring like, with water temperatures close to air temperatures and therefore alternating destabilizing and stabilizing regimes due to the changing buoyancy flux.

Generally the Monin-Obukhov length was much smaller than the Mixed Layer Depth (see for example Figure 3.15d, except for a few days, namely April 19, July 24, September 18, October 20 and January 7 at the Reference Station. The fact that this only occurred several times during the year indicates that buoyancy forces were most of the time dominant in the Well Mixed Layer.
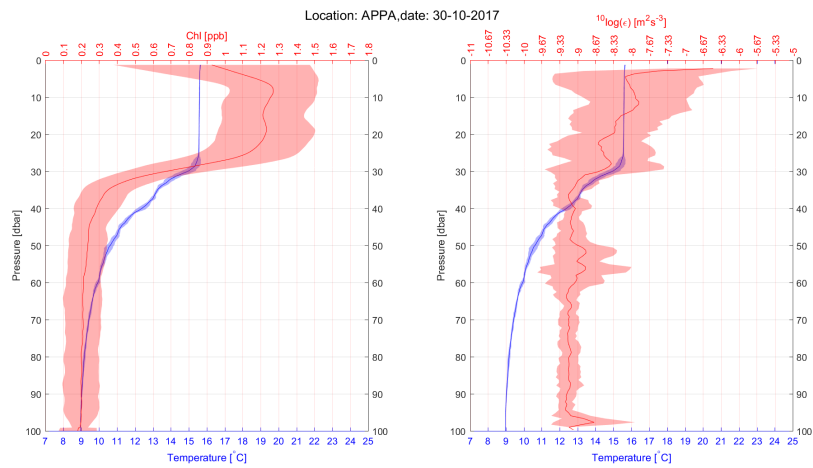
The transition period also marked a transition in the wind patterns. This is shown in Figure 4.3. During the Summer (14 June until 2 September) the wind was primarily from the south (4.3a), while during the transition period (2 September until October 21, 4.3b) it was sometimes from the south en sometimes from the northeast, with weak winds from the southwest. Then, in the autumn and the beginning of the winter (October 21 until January 9, 4.3c) the wind was most of the time either from the south-southwest or from the northeast. There seems to be a relation between the development of the unstable boundary layer over the lake and the local wind pattern. However, it remains unclear if the boundary layer is somehow affecting the local wind pattern or that the wind pattern and the development of this boundary layer are related by an external forcing mechanism.
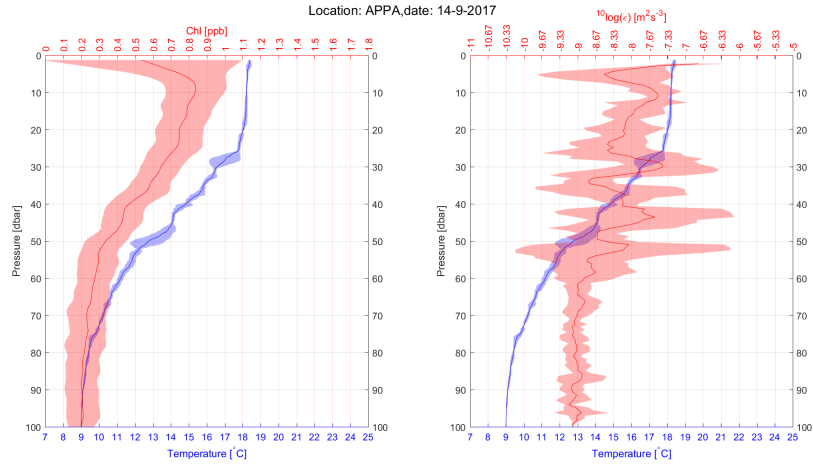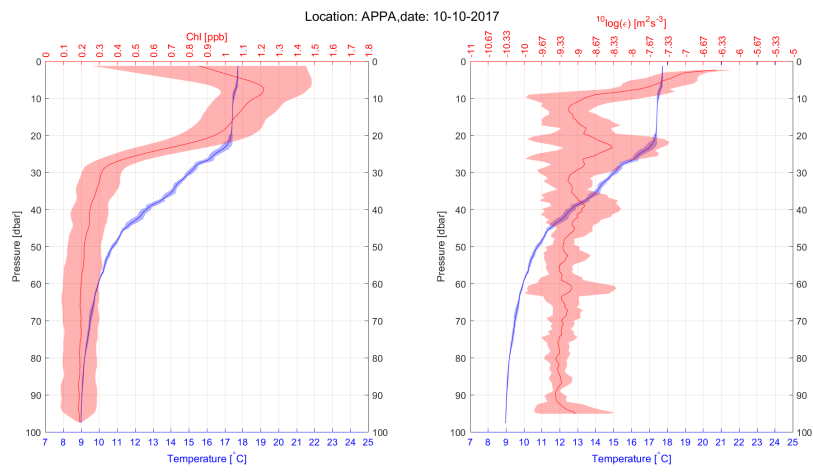
Figure 4.2: *The increase in Chlorophyll-a concentrations at the Reference Station during the transition period in red (on the left). Shown in blue is the temperature. The right figure shows the TKE dissipation in red and temperature in blue. Shown here are three dates: 14 Sep 2017 (a), 10 Oct 2017 (b) and 30 Oct 2017 (c). The shaded areas indicate 95% confidence intervals.*
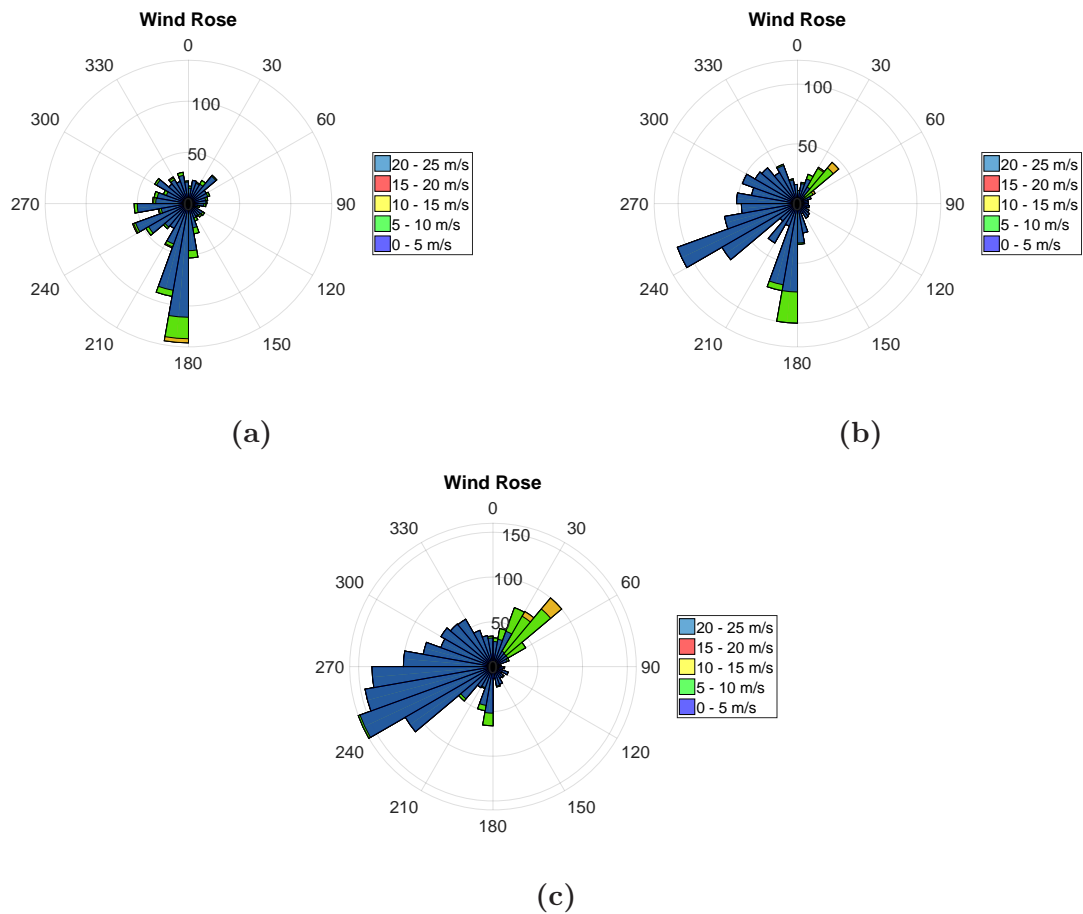
Figure 4.3: *Wind roses for three different periods: **(a)**: 14 June - 2 September 2017, **(b)**: 2 September - 21 October 2017, **(c)**: 21 October 2017 - January 9 2018. The colour indicates the measured wind speed, while the length shows direction and amount of data points collected in the specific bin (radial axis).*

4.3 Thorpe Scale & Dissipation

The values for TKE dissipation range from about 10^{-7} $m^2 s^{-3}$ at the surface to 10^{-9} $m^2 s^{-3}$ at 50 dBar and below. This difference is due to the fact that at the surface turbulence generated by the wind plays a much more prominent role than at greater depths. However, there is no clear seasonality in the dissipation or the vertical mixing coefficient. During June and July intense mixing was observed in the layers around 20 m of depth. The explanation for this remains unclear, but a possibility might be that it has to do with mixing caused by internal waves. During December, January and February mixing was intensified throughout the water column, compared to the months before. Probably because the lake was cooling all the time, causing Mixed Layer deepening. A wind event also took place on January 7, which has probably enhanced the Mixed Layer deepening. The signal of enhanced mixing is also present in the Chlorophyll-a concentrations (Figure 3.9b).

It was found that the dissipation profiles at the Reference Station were not following the Law of the Wall. We might therefore conclude that other processes play a more important role on the lake, like buoyancy. For some days (October 30, April 21 and August 7) there was found less mixing than what would be expected from the wind that was blowing that day.

The Thorpe length (L_T) shows a seasonal cycle, albeit it being relatively subtle and only visible because so many profiles have been taken. Despite the results not being significantly different, it was still observed that the Thorpe scale increased during the winter months and thus that eddies tend to be larger during the winter than during the summer. The biggest difference in the Thorpe length was also found between summer and winter: 0.106 ± 0.019 m in summer and 0.53 ± 0.25 m in the winter.

4.4 Extreme Situations

The mean wind conditions for the days preceding April 21 and August 7 are shown in Figure 4.4. Both on April 21 and August 7, the wind was coming from the northeast in the preceding days. The wind event on August 7 lasted less long, but the winds were a lot stronger than on April 21.

Significant anomalies with respect to the Reference Station were found in the TKE dissipation. These anomalies were most profound on April 21, August 7 and December 13. The anomalies during December are probably due to anomalous low mixing rates below 50 dBar at the Reference station. (Figure 3.15d). The anomalies were mostly found at the Western Station and Limone Station. On April 21 there was significantly intensified mixing at the Eastern Station and not at the Western or Limone Station. The same happened, albeit less intense, on August 7. The same kind of pattern during these days is observed in the temperature profiles. On April 21 and August 7, it was significantly warmer at the Western and Limone Station and significantly colder (Figure A.2) at the Eastern Station. In fact, it was 0.8°C colder at the Eastern Station with respect to the Reference station, and 7 °C and 4.9 °C warmer at the Limone Station and Western Station, respectively, on August 7. Hence, we observe indeed an increased upwelling in the east directly after these wind events on both April 21 and August 7.
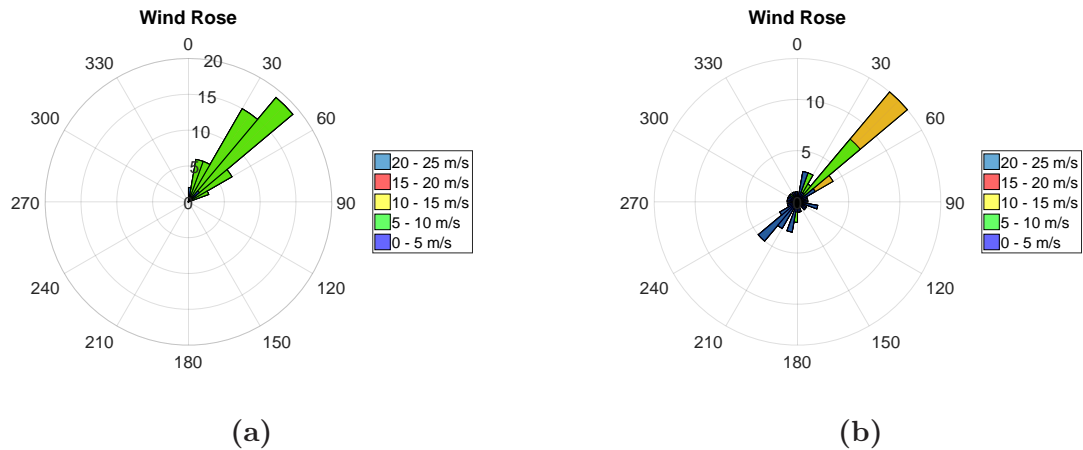
Figure 4.4: *(a): Wind speeds and direction on the three days preceding 21 April. (b): Wind speed and direction on the days preceding 7 August. The colour indicates the measured wind speed, while the length shows direction and amount of data points collected in the specific bin (radial axis).*

This is in accordance with the theory as explained in Section 3.5.1 and there is thus observational evidence of such a circulation.

The chlorophyll-a showed no significant gradients along the transect (see section A.3. The uncertainty is too high, so more precise measurements are needed to indicate whether there is any effect on the chlorophyll-a concentrations. It is clear though, that Limone had higher concentrations of chlorophyll-a during the spring than the Reference Station.

Chapter 5

Conclusion

In this study we have investigated the influence of external forcing on the dynamics of a deep alpine lake (Lake Garda) over a full seasonal cycle. Specifically we have looked at the influence of air temperature, net heat flux and wind on vertical mixing, temperature and chlorophyll-a concentrations.

It was found that throughout the year the buoyancy flux, and thus the net heat flux, is the most important parameter throughout the year. This is reflected in the Law of the Wall scaling, which showed that dissipation in general does not follow this law, but also in the fact that the Monin-Obukhov was most of the time smaller than the Mixed Layer Depth. However, during occasional extreme wind events, significant amounts of TKE were produced and the Monin-Obukhov exceeded the Mixed Layer Depth. Observational evidence has been found that these wind events gave rise to a secondary circulation as discussed by Toffolon [43], causing upwelling in parts of the lake.

It was found that a transition period from negative to positive buoyancy fluxes in the months September and October marked a transition in the wind climate and caused the development of an unstable boundary layer in the air above the lake, but also in the lake itself. It was the onset of Mixed Layer deepening. The development of the unstable boundary layer was caused by the lake surface temperature becoming higher than the air temperature. Furthermore, the transition period was marked by a second algal bloom.

The first algal bloom started at the end of April and led to a maximum being observed on June 13 at the Reference Station, with a concentration of 1.224 ± 0.021 ppb being reached at a depth of 20 dBar. The maximum recorded temperature in the lake was reached a month later on July 13 with a maximum of 22.38 ± 0.09°C at a depth of 5 dBar. The water column was completely mixed on January 24 with a temperature of 9.152 ± 0.001 °C and it would keep cooling down until March 23 with a temperature of 8.779 ± 0.001 °C being reached at 90 m depth that day.

A clear seasonal signal could not be distinguished from the dissipation and vertical mixing profiles, but it was found that during the months December, January and February significant mixing was taking place throughout the water column. This was reflected in the found Mixed Layer Depths, and the increased dissipation during this period. It is therefore likely that a Deep Mixing Event has happened in these months. A clearer seasonal signal was obtained from the Thorpe scale analysis, but the results were not significant, unfortunately. It was found that the Thorpe scale is larger in the winter months than in the summer months, but the spread is also larger. The mean values were 0.106 ± 0.019m and 0.53 ± 0.25m, respectively for the summer months and the winter months.

All in all it can be concluded that most of the time the mixing dynamics seem to be dominated by the bouyancy flux, rather than the wind. The mixing dynamics in Lake Garda are strongly influenced by events occurring over the year and a clear seasonal cycle in the mixing dynamics could not be found.

Bibliography

[1] M. Simona, "Winter and spring mixing depths affect the trophic status and composition of phytoplankton in the northern meromictic basin of Lake Lugano", *Journal of Limnology*, vol. 62, no. 2, pp. 190–206, 2003.

[2] B. Boehrer, R. Fukuyama, K. Chikita, and H. Kikukawa, "Deep water stratification in deep caldera lakes Ikeda, Towada, Tazawa, Kuttara, Toya and Shikotsu", *Limnology*, vol. 10, no. 1, p. 17, 2009.

[3] A. Wüest and A. Lorke, "Small-scale hydrodynamics in lakes", *Annual Review of fluid mechanics*, vol. 35, no. 1, pp. 373–412, 2003.

[4] S. Piccolroaz, M. Toffolon, and B. Majone, "The role of stratification on lakes' thermal response: The case of Lake Superior", *Water Resources Research*, vol. 51, no. 10, pp. 7878–7894, 2015.

[5] B. M. Kraemer, O. Anneville, S. Chandra, M. Dix, E. Kuusisto, D. M. Livingstone, A. Rimmer, S. G. Schladow, E. Silow, L. M. Sitoki, *et al.*, "Morphometry and average temperature affect lake stratification responses to climate change", *Geophysical Research Letters*, vol. 42, no. 12, pp. 4981–4988, 2015.

[6] M. Scheffer, D. Straile, E. H. van Nes, and H. Hosper, "Climatic warming causes regime shifts in lake food webs", *Limnology and Oceanography*, vol. 46, no. 7, pp. 1780–1783, 2001.

[7] W. Bleiker and F. Schanz, "Influence of environmental factors on the phytoplankton spring bloom in lake zürich", *Aquatic Sciences*, vol. 51, no. 1, pp. 47–58, 1989.

[8] F. Peeters, D. Straile, A. Lorke, and D. Ollinger, "Turbulent mixing and phytoplankton spring bloom development in a deep lake", *Limnology and Oceanography*, vol. 52, no. 1, pp. 286–298, 2007.

[9] N. Salmaso, A. Boscaini, C. Capelli, and L. Cerasino, "Ongoing ecological shifts in a large lake are driven by climate change and eutrophication: Evidences from a three-decade study in Lake Garda", *Hydrobiologia*, pp. 1–19, 2017.

[10] N. Salmaso, G. Morabito, R. Mosello, L. Garibaldi, M. Simona, F. Buzzi, and D. Ruggiu, "A synoptic study of phytoplankton in the deep lakes south of the alps (lakes Garda, Iseo, Como, Lugano and Maggiore)", *Journal of Limnology*, vol. 62, no. 2, pp. 207–227, 2003.

[11] W. R. Rouse, C. M. Oswald, J. Binyamin, P. D. Blanken, W. M. Schertzer, and C. Spence, "Interannual and seasonal variability of the surface energy balance and temperature of central Great Slave Lake", *Journal of Hydrometeorology*, vol. 4, no. 4, pp. 720–730, 2003.

[12] J. Michalski and U. Lemmin, "Dynamics of vertical mixing in the hypolimnion of a deep lake: Lake geneva", *Limnology and oceanography*, vol. 40, no. 4, pp. 809–816, 1995.

[13] J. Weck and A. Lorke, "Mixing efficiency in the thermocline of lakes observed from eddy correlation flux measurements", *Journal of Geophysical Research: Oceans*, vol. 122, no. 1, pp. 291–305, 2017.

[14] M. Ventura, L. Camarero, T. Buchaca, F. Bartumeus, D. M. Livingstone, and J. Catalan, "The main features of seasonal variability in the external forcing and dynamics of a deep mountain lake (Redó, Pyrenees)", *Journal of Limnology*, vol. 59, no. 1s, pp. 97–108, 2000.

[15] L. Laiti, D. Zardi, M. de Franceschi, and G. Rampanelli, "Atmospheric boundary layer structures associated with the Ora del Garda wind in the Alps as revealed from airborne and surface measurements", *Atmospheric research*, vol. 132, pp. 473–489, 2013.

[16] N. Salmaso, "Effects of climatic fluctuations and vertical mixing on the interannual trophic variability of Lake Garda, Italy", *Limnology and Oceanography*, vol. 50, no. 2, pp. 553–565, 2005.

[17] C. Giardino, V. E. Brando, A. G. Dekker, N. Strömbeck, and G. Candiani, "Assessment of water quality in Lake Garda (Italy) using Hyperion", *Remote Sensing of Environment*, vol. 109, no. 2, pp. 183–195, 2007.

[18] N. Salmaso, "Ecological patterns of phytoplankton assemblages in Lake Garda: Seasonal, spatial and historical features", *Journal of Limnology*, vol. 61, no. 1, pp. 95–115, 2002.

[19] D. M. Imboden and A. Wüest, "Mixing mechanisms in lakes", in *Physics and chemistry of lakes*, Springer, 1995, pp. 83–138.

[20] G. I. Taylor, "Statistical theory of turbulence", *Proceedings of the Royal Society of London. Series A, Mathematical and Physical Sciences*, vol. 151, no. 873, pp. 421–444, 1935.

[21] T. Osborn, "Estimates of the local rate of vertical diffusion from dissipation measurements", *Journal of Physical Oceanography*, vol. 10, no. 1, pp. 83–89, 1980.

[22] S. R. Brody and M. S. Lozier, "Characterizing upper-ocean mixing and its effect on the spring phytoplankton bloom with in situ data", *ICES Journal of Marine Science*, vol. 72, no. 6, pp. 1961–1970, 2015.

[23] E. Jurado, H. Woerd, and H. Dijkstra, "Microstructure measurements along a quasi-meridional transect in the northeastern Atlantic Ocean", *Journal of Geophysical Research: Oceans*, vol. 117, no. C4, 2012.

[24] C.-T. A. Chen and F. J. Millero, "Thermodynamic properties for natural waters covering only the limnological range", *Limnology and Oceanography*, vol. 31, no. 3, pp. 657–662, 1986.

[25] C. E. Bluteau, N. L. Jones, and G. N. Ivey, "Estimating turbulent dissipation from microstructure shear measurements using maximum likelihood spectral fitting over the inertial and viscous subranges", *Journal of Atmospheric and Oceanic Technology*, vol. 33, no. 4, pp. 713–722, 2016.

[26] T. R. Osborn, "Vertical profiling of velocity microstructure", *Journal of Physical Oceanography*, vol. 4, no. 1, pp. 109–115, 1974.

[27] P. W. Nasmyth, "Oceanic turbulence", PhD thesis, University of British Columbia, 1970.

[28] N. Oakey, "Determination of the rate of dissipation of turbulent energy from simultaneous temperature and velocity shear microstructure measurements", *Journal of Physical Oceanography*, vol. 12, no. 3, pp. 256–271, 1982.

[29] M. Toffolon, S. Piccolroaz, and H. A. Dijkstra, "A Plunge into the Depths of Italy's Lake Garda", *Eos*, vol. 98, 2017.

[30] R. Lueck, "RSI technical note 028: Calculating the Rate of Dissipation of Turbulent Kinetic Energy", 2016.

[31] ——, "RSI technical note 005: Converting shear-probe, thermistor and microconductivity signals into physical units", 2016.

[32] S. Thorpe, "Turbulence and mixing in a Scottish loch", *Phil. Trans. R. Soc. Lond. A*, vol. 286, no. 1334, pp. 125–181, 1977.

[33] S. Kioroglou, E. Tragou, and V. Zervakis, "Assessing shelf mixing using CTD, ADCP, and free falling shear probe turbulence data", *Continental Shelf Research*, vol. 69, pp. 73–87, 2013.

[34] T. Dillon, "Vertical overturns: A comparison of Thorpe and Ozmidov length scales", *Journal of Geophysical Research: Oceans*, vol. 87, no. C12, pp. 9601–9613, 1982.

[35] H. L. Bryden, "New polynomials for thermal expansion, adiabatic temperature gradient and potential temperature of sea water", in *Deep Sea Research and Oceanographic Abstracts*, Elsevier, vol. 20, 1973, pp. 401–408.

[36] K. Stansfield, C. Garrett, and R. Dewey, "The probability distribution of the Thorpe displacement within overturns in Juan de Fuca Strait", *Journal of physical oceanography*, vol. 31, no. 12, pp. 3421–3434, 2001.

[37] B. Ferron, H. Mercier, K. Speer, A. Gargett, and K. Polzin, "Mixing in the Romanche fracture zone", *Journal of Physical Oceanography*, vol. 28, no. 10, pp. 1929–1945, 1998.

[38] P. S. Galbraith and D. E. Kelley, "Identifying overturns in CTD profiles", *Journal of Atmospheric and Oceanic Technology*, vol. 13, no. 3, pp. 688–702, 1996.

[39] H. L. Johnson and C. Garrett, "Effects of noise on Thorpe scales and run lengths", *Journal of physical oceanography*, vol. 34, no. 11, pp. 2359–2372, 2004.

[40] R. I. Woolway, I. D. Jones, D. P. Hamilton, S. C. Maberly, K. Muraoka, J. S. Read, R. L. Smyth, and L. A. Winslow, "Automated calculation of surface energy fluxes with high-frequency lake buoy data", *Environmental Modelling & Software*, vol. 70, pp. 191–198, 2015.

[41] S. Piccolroaz, M. Toffolon, and B. Majone, "A simple lumped model to convert air temperature into surface water temperature in lakes", *Hydrology and Earth System Sciences*, vol. 17, no. 8, pp. 3323–3338, 2013.

[42] S. A. Thorpe, *An introduction to ocean turbulence.* Cambridge University Press, 2007.

[43] M. Toffolon, "Ekman circulation and downwelling in narrow lakes", *Advances in water resources*, vol. 53, pp. 76–86, 2013.
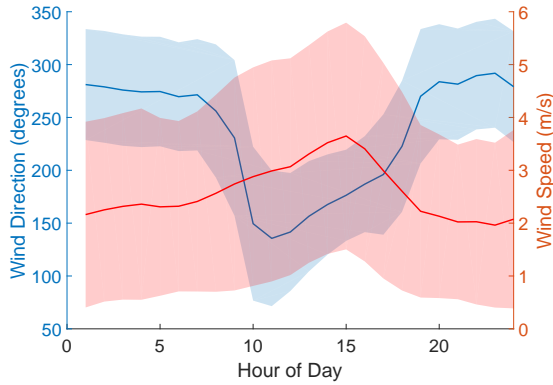
Appendix A

Daily cycle and anomalies

A.1 Daily cycle of wind

Figure A.1: *The average daily cycle of wind direction as measured in the period 7 March 2017 to 7 March 2018. The shaded areas indicate the standard deviation.*

It was found that the wind direction has a daily cycle, averaged over the year, as well. This can be seen in Figure A.1. Generally the winds are from the West during the night, but during the morning the wind starts changing direction and changes by about 120°. The wind thus changes direction to a southeast direction. After this initial rapid change in the wind direction, the wind typically starts turning back slowly again during the day and experiences a maximum wind speed around 15.00 h of about 3.5 ms^{-1}. [1]

A.2 Temperature anomalies

Figure A.2 shows the temperature anomalies with respect to the RS. The contours in Figures A.2a, A.2b and A.2c indicate levels of significant deviation. There were significant difference found throughout the year. On April 21, it was significantly warmer at LS and WS compared to RS, however, at ES the situation was the opposite. It was significantly colder than at RS on this day over the whole water column. The same situation occurred in March, but also in August. But, on August 7, the temperature anomalies were confined to the upper 20-30 dBar of the water column. During October the situation was reversed and it was a significantly colder at the stations of Limone and West station, while it was significantly warmer at the East station at depths upto 20m. At Limone the observed effect was less strong and reached a depth of just 10m. During November the pattern reversed, but now to depths of 50 dBar at ES and 70-80 dBar at WS and LS.

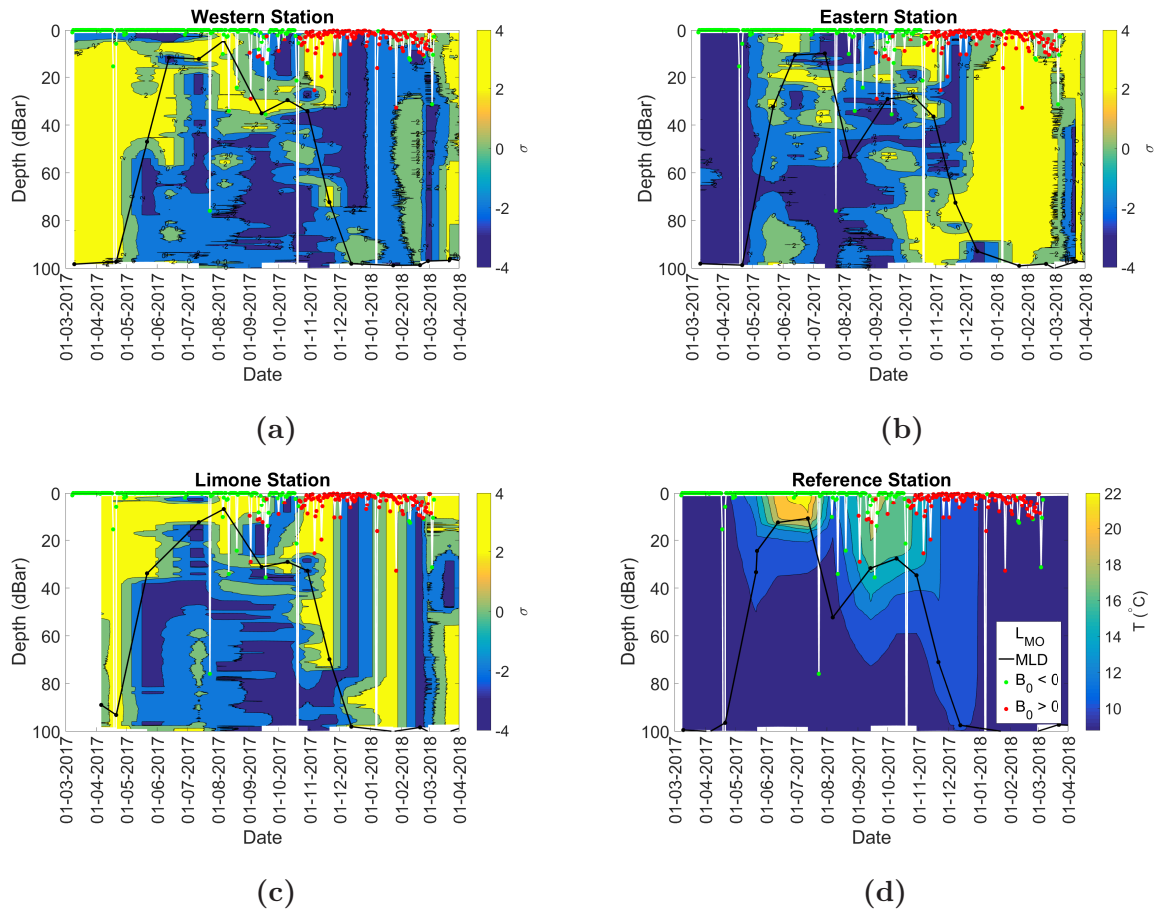[1] All measurements on the lake were carried out between 10 and 15 o'clock.

Figure A.2: *Relative anomalies of temperature in terms of standard deviations, σ, for the stations: **(a)** West, **(b)** East, **(c)** Limone. The contour intervals are two standard deviations. Figure **(d)** shows the temperature in °C at the Reference station. The contour plots were made by using linear interpolation between measurement days.*
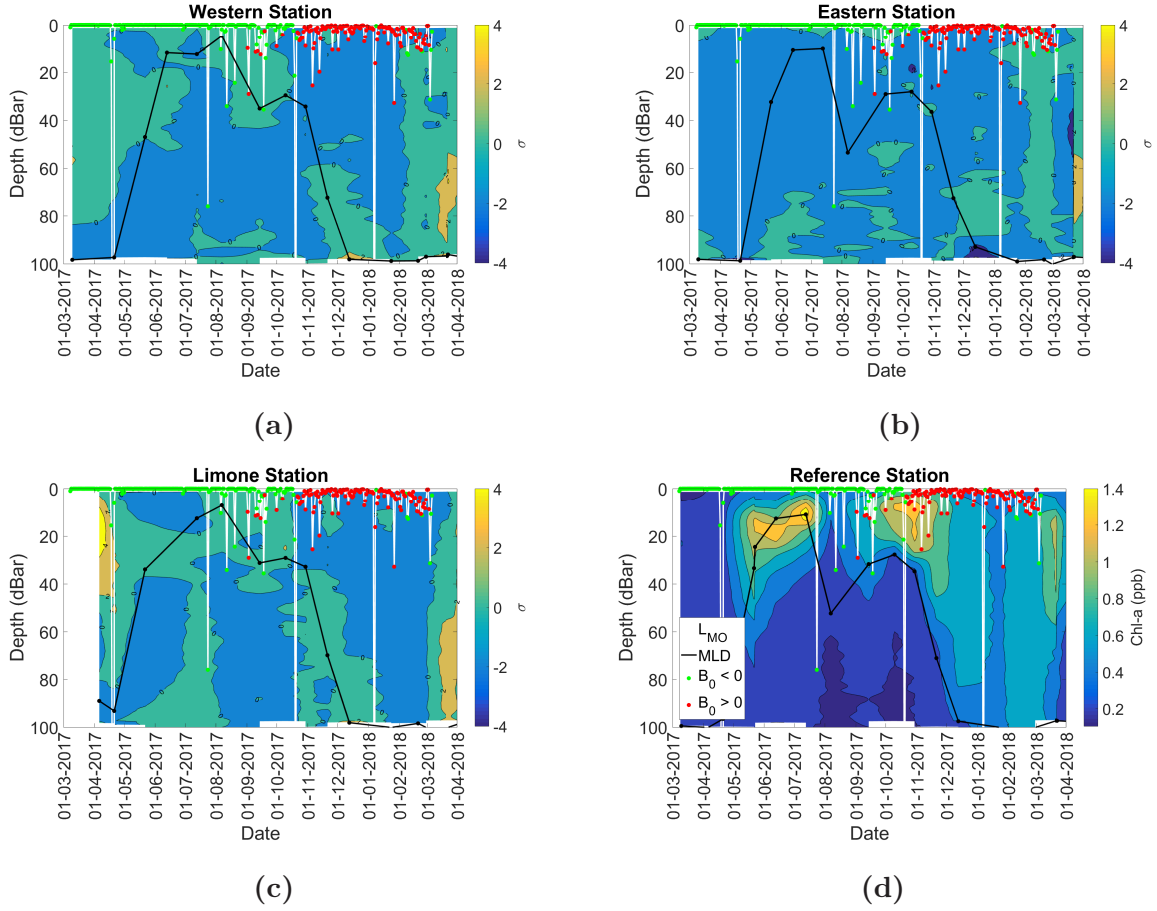
A.3 Chlorophyll-*a* anomalies

Figure A.3: *Relative anomalies of chl-a in terms of standard deviations, σ, for the stations: (a) West, (b) East,(c) Limone. The contour intervals are two standard deviations. Figure (d) shows the concentration in ppb at the Reference station. The black line indicates the Mixed Layer Depth, with the black dots showing the individual measurements. The white lines indicate the Monin-Obukhov length (L_{MO}). Here, a green dot indicates that the buoyancy flux was stabilizing, while a red dot indicates destabilizing. The contour plots were made by using linear interpolation between measurement days.*

Figure A.3 show the relative deviations from the Reference Station in Chlorophyll-*a* concentrations. The contours in Figures A.3a,A.3b and A.3c indicate levels of deviation.

There are very few significant differences at the other stations in Chlorophyll-*a* concentration compared to the Reference Station. The only significant differences are found during the spring. On April 6, 2017, the concentration of Chl-*a* was significantly higher in the upper 40 dBar at the Limone station. The same thing happened in the next spring. On March 23 a significant increase was found below 50 dBar.
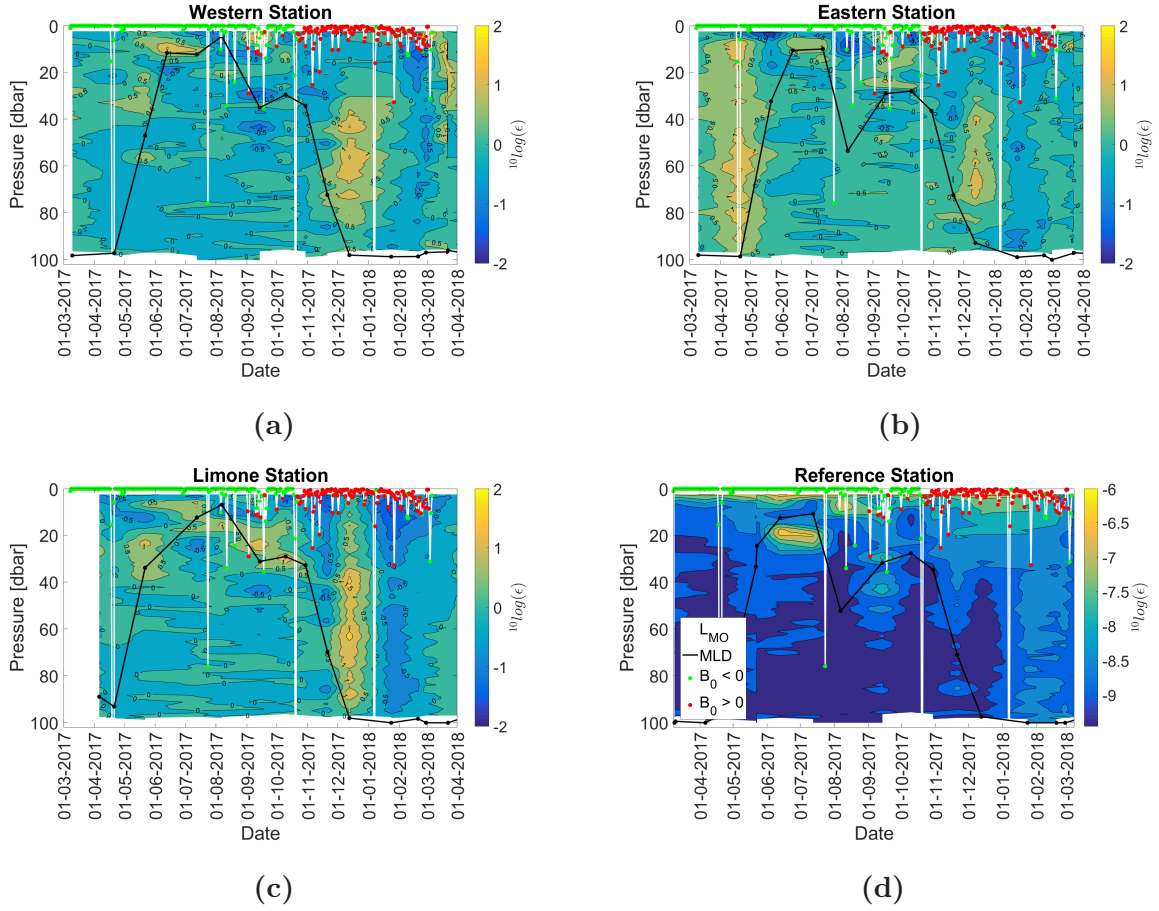
A.4 Absolute Anomalies

Figure A.4: *Absolute anomalies of TKE dissipation in terms of $^{10}\log(\epsilon)$, for the stations: **(a)** West, **(b)** East, **(c)** Limone. The contour intervals are two standard deviations. Figure **(d)** shows the TKE dissipation in $^{10}\log(\epsilon)$ at the Reference station. The black line indicates the Mixed Layer Depth, with the black dots showing the individual measurements. The white lines indicate the Monin-Obukhov length (L_{MO}). Here, a green dot indicates that the buoyancy flux was stabilizing, while a red dot indicates destabilizing. The contour plots were made by using linear interpolation between measurement days.*
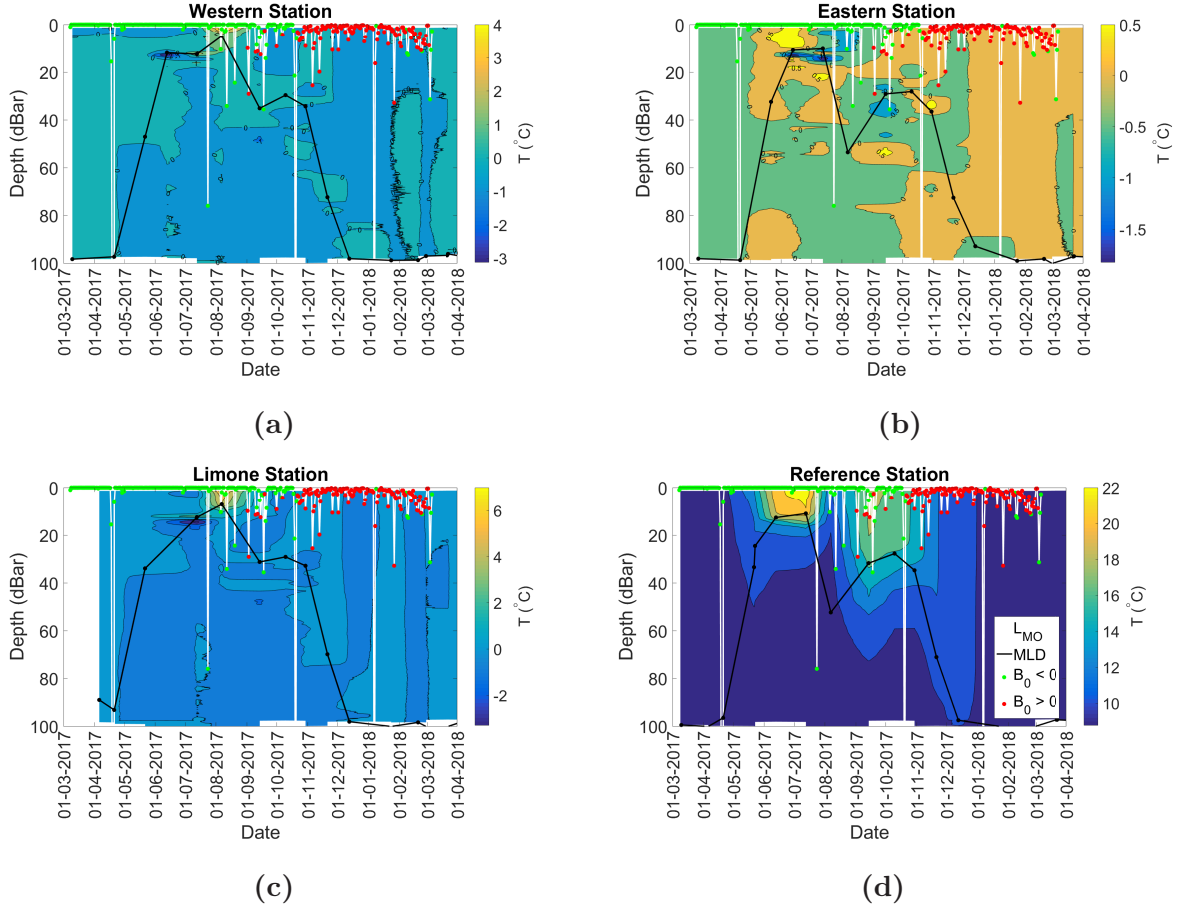
Figure A.5: *Absolute anomalies of temperature in in terms of °C, for the stations: (a) West, (b) East,(c) Limone. The contour intervals are two standard deviations. Figure (d) shows the temperature in °C at the Reference station. The black line indicates the Mixed Layer Depth, with the black dots showing the individual measurements. The white lines indicate the Monin-Obukhov length (L_{MO}). Here, a green dot indicates that the buoyancy flux was stabilizing, while a red dot indicates destabilizing. The contour plots were made by using linear interpolation between measurement days.*
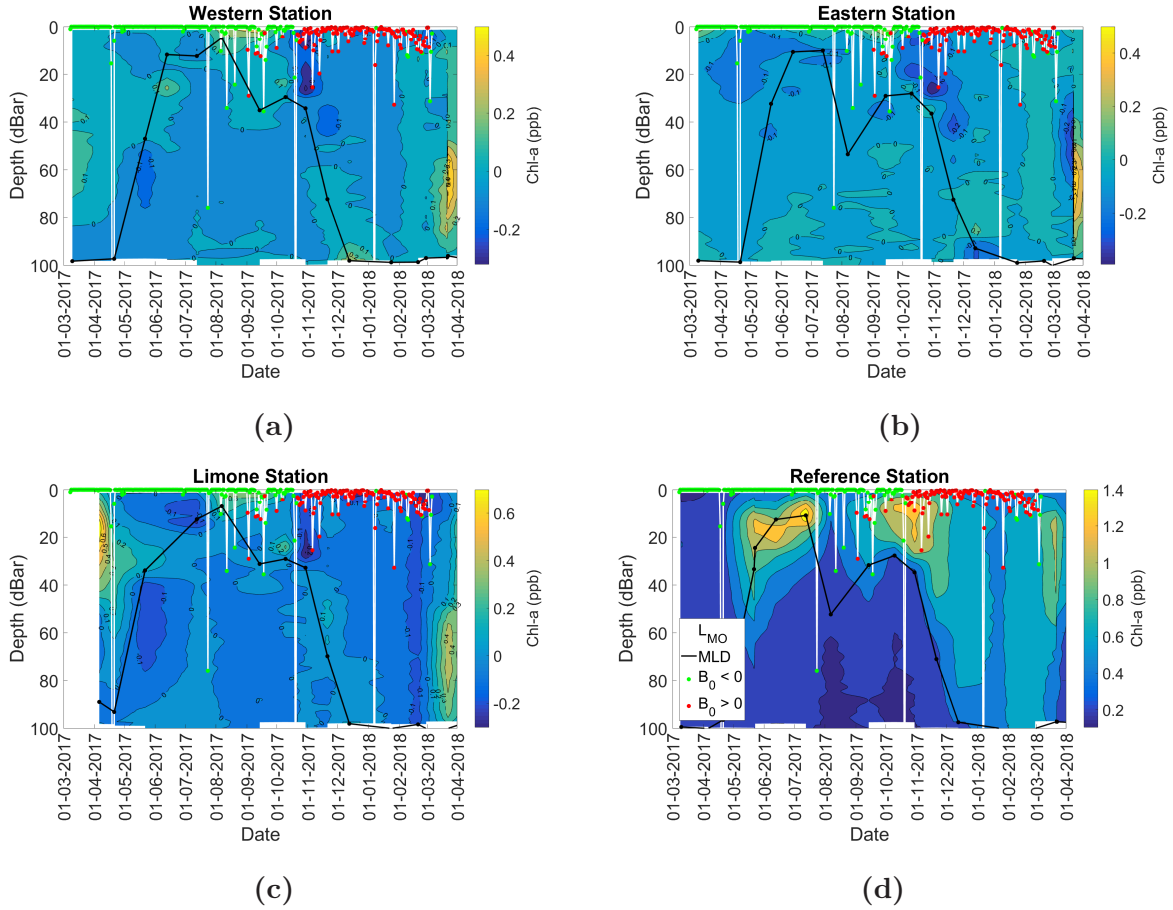
Figure A.6: *Absolute anomalies of chl-a in in terms of ppb, for the stations: **(a)** West, **(b)** East, **(c)** Limone. The contour intervals are two standard deviations. Figure **(d)** shows the chl-a in ppb at the Reference station. The black line indicates the Mixed Layer Depth, with the black dots showing the individual measurements. The white lines indicate the Monin-Obukhov length (L_{MO}). Here, a green dot indicates that the buoyancy flux was stabilizing, while a red dot indicates destabilizing. The contour plots were made by using linear interpolation between measurement days.*